Geophys. J. R. astr. Soc. (1982) **70**, 667–715

On the evolution of rifted continental margins: comparison of models and observations for the Nova Scotian margin

Christopher Beaumont *Department of Oceanography, Dalhousie University, Halifax, Nova Scotia B3H 4J1, Canada*

Charlotte E. Keen *Atlantic Geoscience Centre, Geological Survey of Canada, Bedford Institute of Oceanography, Dartmouth, Nova Scotia B2Y 4A2, Canada*

Ross Boutilier *Department of Oceanography, Dalhousie University, Halifax, Nova Scotia B3H 4J1, Canada*

Received 1981 November 30; in original form 1981 June 2

Summary. A model for the formation and evolution of rifted continental margins based on lithospheric extension during rifting and its thermal and mechanical consequences is proposed. Model predictions are then compared with geological and geophysical observations from a transect of the ~185 Ma old rifted margin off Nova Scotia through the Scotian Basin.

Three kinematic models of the rifting process are discussed. These are: (1) the uniform extension model, in which the amount of extension is uniform with depth but varies with position across the margin; (2) the uniform extension and melt segregation model which has similar properties, but also provides an explanation for the properties of the extended continental crust and its transition to oceanic crust by postulating that basaltic melt segregates from the asthenosphere and migrates to the crust, and; (3) the depth-dependent extension model in which the first-order consequences of rapidly changing rheological properties with depth in the lithosphere are included by decoupling the lithosphere into two zones with depth, each of which undergoes differing amounts of extension.

These rift models predict the form of crustal and lithospheric thinning, subsidence and temperature change once the amount of extension has been determined. This is estimated from seismic measurements of present crustal thickness on the assumption that the crust had a uniform thickness, equal to that currently measured in the adjacent continental region, before rifting occurred. Rifting is also considered to occur instantaneously.

A time-stepping thermo-mechanical model is used to predict the cooling of rifted margin, additional thermal contraction subsidence and its amplification by water and sediment loading. Thermal aspects are calculated using a finite difference model of time-dependent conductive heat transport, whereas regional isostatic response to loading is calculated by a finite element

model. The models are coupled because the temperature distribution is used to define a rheological lithosphere (an elastic region with thickness that varies in time and space as the model evolves) for flexural calculations in the mechanical model. Secondary coupling occurs through perturbations to the temperature field by sedimentary thermal blanketing and advection of heat during isostatic adjustment.

The model predictions of: (1) sedimentary basin stratigraphy, (2) Moho position, (3) free air gravity anomaly, (4) age–depth relations for deep exploratory wells and (5) subsidence and temperature histories agree well with observations from the Scotian Basin. Additional effects due to sedimentary and crustal radiogenic heat production, lateral heat transport and the possible existence of a near surface brittle listric faulted region created during rifting are also considered. It is concluded that a model in which rifting occurred by depth-dependent extension, and which includes a finite thickness for the rheological lithosphere, radiogenic heat production in the sediments and crust, and a brittle listric faulted crustal layer affords an accurate description of the first-order processes that occur during rifting and evolution of this margin.

1 Introduction

Most continental margins created during rifting of a continental lithospheric plate evolve into deep sedimentary basins occupying the transitional region between oceans and continents. These rifted margins, sometimes called Atlantic-type or passive margins, are the subject of intense research interest because they may contain significant hydrocarbon resources. Of the possible mechanisms responsible for their formation and subsequent evolution, the proposal that there is significant horizontal extension during rifting which thins both the crust and subcrustal lithosphere can explain most of the first-order properties of the margins and can be tested by modelling. These properties include: the thinning of the crust landward of the ocean–continent boundary (Sheridan *et al.* 1979; Montadert *et al.* 1979; Keen & Hyndman 1979), subsidence (Sleep 1971; Watts & Steckler 1979; Watts & Ryan 1976; Keen 1979; Royden & Keen 1980), and listric faulting of the upper crust (Montadert *et al.* 1979).

The intention of this paper is to explore the consequences of extensional models of rifting with particular reference to the rifting process, the post-rift cooling, thermal contraction and subsidence of the lithosphere, and the amplification of this subsidence by sediment and water loads. Three kinematic models of rifting: the uniform extension model, the uniform extension and melt segregation model and the depth-dependent extension model, are examined in detail. These processes control the post-rifting history, which is traced by a thermo-mechanical model in which subsidence and temperature are the result of conductive cooling, and the isostatic response to loading by sediment and water is found by assuming these loads are supported by an elastic layer. The models are coupled in that the space available for sediments and water depends on the thermal history, and the thickness of the elastic layer, termed the rheological lithosphere, in the mechanical model is determined by the temperature distribution. Arguments are presented that justify the mechanical model by comparison with thermally activated creep mechanisms of rocks observed in laboratory experiments. Additional feedback due to thermal blanketing of the sediments and sediment compaction is included in the models.

The two-dimensional models predict the form of cross-sections of continental margins that can be compared with observations. In this paper results are compared with a cross-

section of the ~185 Ma old Nova Scotia margin that passes through the deepest part of the Scotian Basin. The amount of crustal extension is estimated from the seismic measurements of the present crustal thickness assuming that prior to rifting the crust had a uniform thickness equal to the present thickness at the landward end of the section. The sediment budget was calculated by decompacting the observed stratigraphic section.

The success of the models is assessed on the basis of: (1) the ability of the model basin to accommodate the prescribed sediment for each timestep while maintaining reasonable palaeobathymetries; (2) the ability of the model to predict accurate age–depth relationships for sample exploratory wells along the section; (3) the accuracy of the disposition of sediment and basement interfaces in the final model; (4) the accuracy of model free air gravity anomalies; and (5) the accuracy of the predicted temperature distribution.

It is shown how subsidence and thermal histories for the sediments may be calculated as a prelude to estimating levels of thermal metamorphism of organic material within the sedimentary section.

Additional effects due to crustal and sedimentary radiogenic heat production and the possible existence of a near surface brittle fractured layer of the crust created during rifting are also considered.

2 Models of lithospheric extension during rifting

The models of rifting discussed in this paper (Fig. 1) are based on the proposal that during the process which leads to continental separation and the formation of oceanic lithosphere,

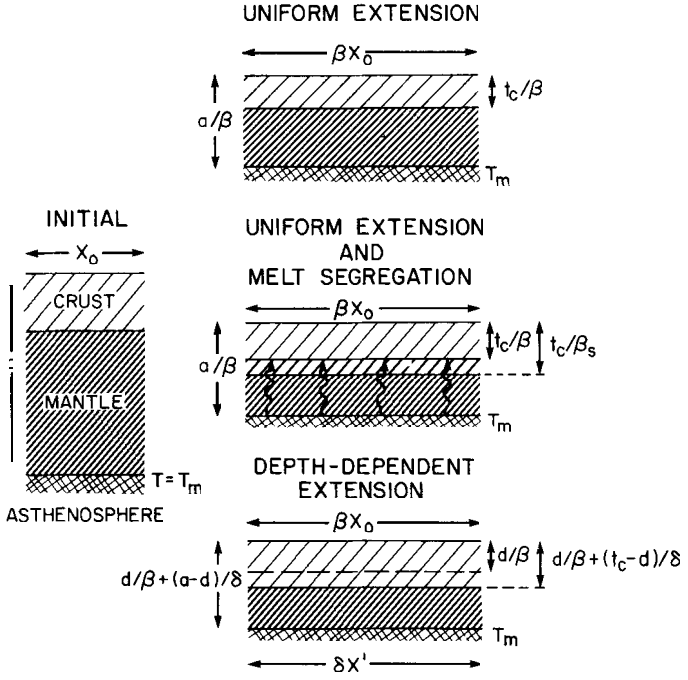

Figure 1. One-dimensional illustrations of the three rifting processes discussed. A segment of the lithosphere of initial length x_0 and depth a is extended by β in the uniform extension model. The other two models include the possibility that segregated melt from the asthenosphere migrates to the extended crust, and that the amount of extension may change with depth in the lithosphere. The temperature of the asthenosphere is T_m, t_c is the initial crustal thickness, d is the depth at which extension changes from β to δ, and t_c/β_s is the final thickness of the crust when segregated melt is included (see Fig. 3).

there is significant extension or stretching of the continental lithosphere. The amount of extension β, progressively increases across the mirrored embryonic margins (Fig. 2) to a value at which the process of tensional stress release changes from stretching of the continental lithosphere to rupture and accretion of oceanic lithosphere. At this point the rifting process is complete.

The consequences of extension during rifting are conceptually simple. The crust and subcrustal lithosphere are initially thinned by β, and the space created filled by the passive upwelling of hot asthenosphere (Figs 1 and 2). Extension will therefore be accompanied by isostatic elevation changes due to replacement of thin crust by mantle lithosphere, and density changes due to heating and thermal expansion. Longer-term subsidence will occur

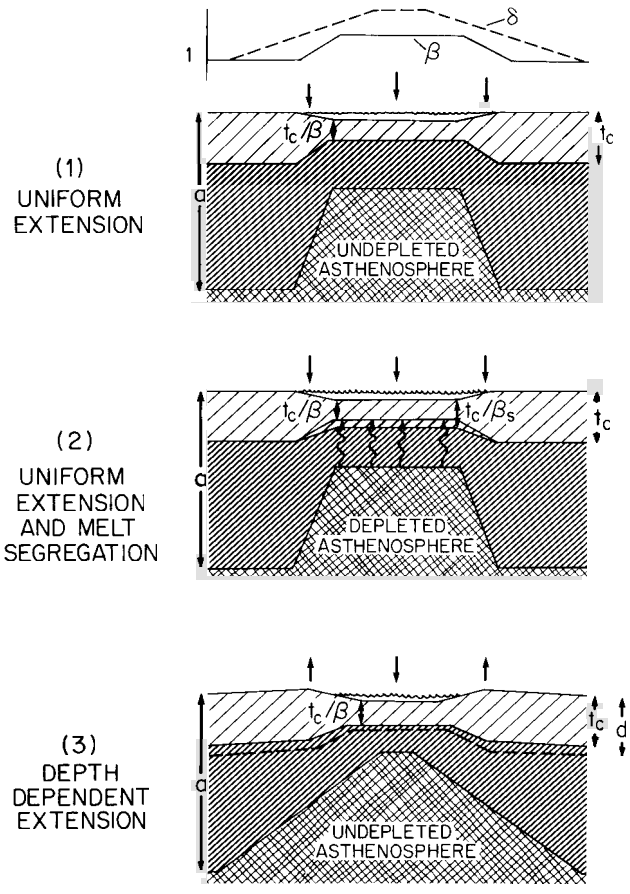

Figure 2. Two-dimensional cross-sections showing lithospheric extension during rifting for the three rifting models. In the uniform extension model both crust and lithosphere are extended and thinned by β, with β varying with position as shown in the upper panel. Initial subsidence occurs for all regions where $\beta > 1$. Extended lithosphere is replaced by the passive upwelling of undepleted asthenosphere. Similar extension by β occurs in the uniform extension and melt segregation model. However, the extended crust is thickened by basaltic melt that segregates from the incoming asthenosphere. This melt is shown underplating the crust but can equally well be considered to intrude it. In the depth-dependent extension model an upper layer $z \leqslant d$ is extended by β whereas the layer beneath $z = d$ is extended by δ as shown in the upper panel. d may be greater or less than the initial crustal thickness, t_c. Such a model can give initial uplift, for regions where β is small, as well as subsidence where β and δ are large. No melt segregation is postulated.

Table 1. Parameter and property values for models.

(1) *Water layer*

Density of seawater (ρ_w) 1030 kg m^{-3}

(2) *Sediments*

	Sandstone	Shale	Limestone	Salt
Matrix density (ρ_{sg}) (kg m^{-3})	2650	2700	2710	2160
Compaction constant (h) (m^{-1})	360	650	160	∞
Surface porosity (ϕ_0) (per cent)	62	60	24	0
Thermal conductivity (K)				
(W m^{-1} °C^{-1})	4.184	1.883	2.929	5.858
(cal cm^{-1} s^{-1} °C^{-1}) ($\times 10^{-3}$)	10	4.5	7	14
Specific heat (c)				
(J kg^{-1} °C^{-1})	1088	837	1004	854
(cal g^{-1} °C^{-1})	0.26	0.20	0.24	0.204
Radioactive heat production (A)				
(μW m^{-3})	0.8368	1.046	0.8368	0
(cal cm^{-3} s^{-1}) ($\times 10^{-13}$)	2	2.5	2.0	0

Volume coefficient of thermal expansion (α) 3.2×10^{-5} °C^{-1}

(3) *Crust*

Pre-rift thickness (t_c) 35 km
Density (ρ_c) 2819.882 kg m^{-3}
Thermal conductivity (K) 3.099 W m^{-1} °C^{-1}
7.407 $\times 10^{-3}$ cal cm^{-1} s^{-1} °C^{-1}
Specific heat at constant volume × density (ρc) 3.877 $\times 10^{6}$ J m^{-3} °C^{-1}
0.9266 cal cm^{-3} °C^{-1}
Radioactive heat production (A) 2.092 μW m^{-3}
5 $\times 10^{-13}$ cal cm^{-3} s^{-1}
Volume coefficient of thermal expansion (α) 3.2 $\times 10^{-5}$ °C^{-1}
Depth of brittle layer (d) 35 km
Depth of radioactive layer of uniform density (b) 7.5 km

(4) *Subcrustal lithosphere*

Pre-rift thickness ($a - t_c$) 125–35 = 90 km
Density (ρ_0) 3330 kg m^{-3}
Thermal conductivity (K) 3.099 W m^{-1} °C^{-1}
7.407 $\times 10^{-3}$ cal cm^{-1} s^{-1} °C^{-1}
Specific heat at constant volume × density (ρc) 3.877 $\times 10^{6}$ J m^{-3} °C^{-1}
0.9266 cal cm^{-3} °C^{-1}
Volume coefficient of thermal expansion (α) 3.2 $\times 10^{-5}$ °C^{-1}

(5) *Asthenosphere*

Density (ρ_0') 3186 kg m^{-3}
Temperature (T_m) 1350°C
Thermal conductivity (K) 3.099 W m^{-1} °C^{-1}
7.047 $\times 10^{-3}$ cal^{-1} cm^{-1} s^{-1} °C^{-1}
Specific heat at constant volume × density (ρc) 3.877 $\times 10^{6}$ J m^{-3} °C^{-1}
0.9266 cal cm^{-3} °C^{-1}
Volume coefficient of thermal expansion (α) 3.2 $\times 10^{-5}$ °C^{-1}

(6) *Rheological lithosphere*

Relaxation isotherm (T_R) 0, 250, 450°C
Young's modulus (E) 2 $\times 10^{11}$ Pa
Poisson's ratio (ν) 0.25
Density of underlying fluid (ρ_f) 3186 kg m^{-3}

(7) *Thermo-mechanical model*

Timestep in finite difference thermal model (Δt) 0.1 Ma
Grid size in finite difference thermal model (Δz) 0.5 km

as the extended region of the margin conductively cools and undergoes thermal contraction. This subsidence is analogous to that of oceanic lithosphere as it migrates from an oceanic ridge (Parsons & Sclater 1977). Extension is assumed to occur on a sufficiently short geological time-scale that it can be modelled as an instantaneous process without significant error (Jarvis & McKenzie 1980). The consequences of this assumption, which is valid if rifting spans an interval that is short in comparison with the lithospheric thermal time constant, are discussed later in this paper.

The immediate elevation change, during extension, is treated as a local isostatic process. It is termed the initial subsidence, S_I, and the longer-term subsidence is the thermal contraction subsidence, S_C. Together, they constitute the tectonic subsidence, S_T, as distinct from the additional isostatic subsidence in response to loading by sediments and water, or the erosion of uplifts.

The cause of extension and details of the rheological response during extension are, as yet, poorly understood but an approximate analogy is thought to be necking of metals when drawn with brittle and ductile failure in cold and hot regions respectively. The kinematic models employed do not require that these properties be known, although some consequences of brittle versus ductile extension are considered later. The tectonic subsidence and the thermal history can be calculated if the amount of extension as a function of horizontal coordinate position, $\beta(x)$, has been specified. It is assumed that mass and heat energy of the lithosphere are conserved during extension; local isostatic equilibrium is maintained during rifting and the initial thickness of the crust (t_c) and lithosphere (a) defined by the solidus temperature (T_m), mean densities (ρ_c, ρ_0) and their expansion coefficients (α), are known (Table 1).

2.1 THE UNIFORM EXTENSION MODEL

The most simple one-dimensional model of instantaneous lithospheric extension (McKenzie 1978) requires that extension, β, is uniform throughout the lithosphere and that it does not change laterally (Fig. 1). The model can be used as a good approximation to extension of continental margins if variations in β from unmodified continent ($\beta = 1$) to ocean ($\beta \to \infty$) (Fig. 2) have a sufficiently small gradient to preclude significant lateral heat transport during cooling. That this is true to first order is demonstrated in Appendix A. Therefore, lateral variations in β are included in the models by interpolating between one-dimensional solutions for temperature and tectonic subsidence.

The initial subsidence (McKenzie 1978; as corrected by Royden, Sclater & Von Herzen 1980) and rewritten in terms of average densities without water loading is

$$S_I[\beta(x), t = 0^+] = \left\{ a - \frac{\rho_{cav} t_c + \rho_{0av}(a - t_c)}{\rho_0'} \right\} \left(1 - \frac{1}{\beta}\right),$$

where

$$\rho_{cav} = \rho_c(1 - \alpha T_{cav}),$$

the average density of the crust;

$$\rho_{0av} = \rho_0(1 - \alpha T_{0av}),$$

the average density of subcrustal lithosphere;

$$\rho_0' = \rho_0(1 - \alpha T_m),$$

the density of lithosphere at the solidus;

$$T_{cav} = \frac{T_m}{2}\frac{t_c}{a},$$

the average temperature of the crust; and

$$T_{0av} = \frac{T_m}{2}\left(1 + \frac{t_c}{a}\right),$$

the average temperature of subcrustal lithosphere, and a zero pre-rift freeboard of the continent is assumed. For a reasonable choice of densities and initial crustal thickness, subsidence, in response to the replacement of low density crust by high density mantle, dominates uplift, caused by the replacement of cold lithosphere by hot asthenosphere. The amount of subsidence is a sensitive function of the chosen densities. Uncertainties in our knowledge of the true densities, therefore, inevitably limit the accuracy of model predictions of overall subsidence.

Cooling and contraction give an additional thermal subsidence with an asymptotic value as $t \to \infty$ which is a function of the pre- and post-rift temperature distribution,

$$S_C[\beta(x), t \to \infty] = \frac{(a - S_I)\,\alpha(T_{iav} - T_{fav})}{(1 - \alpha T_{fav})},$$

where

$$T_{iav} = \frac{1}{a - S_I}\left\{\frac{\alpha T_m}{2\beta} + \left(a - \frac{a}{\beta} - S_I\right)T_m\right\}, \quad T_{fav} = \frac{T_m}{2}.$$

In this case the expression simplifies to

$$S_C[\beta(x), t \to \infty] = \frac{\alpha T_m}{2 - \alpha T_m}\left\{a\left(1 - \frac{1}{\beta}\right) - S_I\right\}$$

and subsidence occurs with a lithospheric thermal time constant $\tau = a^2/\pi^2\kappa$, where $\kappa = K/\rho c$ is the thermal diffusivity, and K = thermal conductivity, ρ = density and c = specific heat at constant pressure. $S_T(\beta \to \infty,\ t \to \infty) \sim 5450$ m for $a = 125$ km, $\rho_c = 2820$ kg m^{-3}, $\rho_0 = 3330$ kg m^{-3}, $t_c = 35$ km and $\alpha = 3.2 \times 10^{-5}$ °C^{-1}. This depression when instantaneously filled with sediments of mean density $\rho_s = 2400$ kg m^{-3} would initially yield a basin ~22 000 m deep if departures from local isostatic equilibrium and the effects of thermal blanketing by the sediments are ignored.

2.2 THE UNIFORM EXTENSION AND MELT SEGREGATION MODEL

The uniform extension model does not address problems of the formation of oceanic crust and the nature of the continental to oceanic crustal transition. In the $\beta \to \infty$ limit continental crust and lithosphere are totally destroyed and replaced by asthenosphere at the solidus. If the 0°C density of this asthenospheric material is assumed to be the same as that of the lithosphere, the model predicts an excessively large initial subsidence for the oceanic region. For this reason Keen, Beaumont & Boutilier (1981) assumed in their preliminary models that $\beta_{max} = 10$ and that oceanic crust and lithosphere could be approximately equated with continental crust that had been thinned by a factor of 10. The justification for this approximation is that the value $\beta = 10$, when combined with reasonable physical properties of the lithosphere (see Table 1), leads to an initial water loaded subsidence of 2660 m, equal to the

depth of newly formed oceanic crust at mid-ocean ridges. However, the water loaded subsidence for this choice of β underestimates the depth of old ocean basins as $t \to \infty$ because there is insufficient thermal contraction.

The uniform extension and melt segregation model outlined by Keen, Beaumont & Boutilier (1982) addresses the problem of creation of the oceanic crust by assuming that, as before, crust and lithosphere are uniformly extended by β but in addition a fraction of basaltic melt segregates from asthenospheric material brought in to replace extended lithosphere (Figs 1 and 2). Where $\beta \to \infty$ the segregated melt forms the oceanic crust, elsewhere the melt passes through the stretched lithosphere, by virtue of its low density, and can either be considered to intrude the overlying crust or to underplate it. The difference between these two variants of the model is, to first order, a thermal difference approximately equivalent to the difference between the stretching and melt intrusion models of Royden *et al.* (1980). They showed that the differences are detectable only during the early cooling history because the intrusion model initially cools more rapidly.

The melt segregation models used in this paper assume for simplicity of calculation that the melt does not advect heat and that it underplates the extended crust. However, we prefer the geological interpretation that the bulk of the melt probably intrudes the crust which has a nearly equal density. On first inspection it would appear that the melt segregation model would involve many more parameters and would, for this reason, be less desirable than the uniform extension model, but this is not so. Model parameters are chosen so that $\beta = \infty$, $t = 0^+$ produces oceanic crust of thickness, $t_{oc} = 6.5$ km and initial subsidence S_m ($\simeq 1.78$ km) equal to the average depth of mid-ocean ridges with the water load removed. The incoming asthenosphere is assumed to have a 0°C density of ρ_u. It then undergoes segregation to produce oceanic crust with 0°C density equal to that of continental crust, ρ_c, and to leave behind depleted asthenosphere with 0°C density ρ_0 equal to that of the unextended lithosphere. The only unknown is ρ_u which can be found from a mass balance between unsegregated and segregated states since the isostatic balance is unaffected by this process if no heat is advected.

$$\rho_u = \frac{t_{oc}\rho_c + (a - t_{oc} - S_m)\rho_0}{a - S_m}.$$

The initial subsidence is given by;

$$S_I(\beta, t = 0^+) = \left\{\frac{a - (a - t_c)\rho_{0av} - t_c\rho_{cav}}{\rho_u'}\right\}\left(1 - \frac{1}{\beta}\right)$$

where $\rho_u' = \rho_u(1 - \alpha T_m)$, the density of undepleted asthenosphere at the solidus; $\rho_{0av} = \rho_0[1 - \alpha T_m/2(1 + t_c/a)]$, the average density of the extended mantle component of the lithosphere, and $\rho_{cav} = \rho_c(1 - \alpha t_c T_m/2a)$, the average density of the extended crust. The model is obviously an oversimplification in that it ignores phase changes and other possible complexities of the intrusion process but it is thought to be a significantly better approximation in and near the oceanic region than the uniform extension model.

The remaining significant difference from the uniform extension model is that the crust, both oceanic and transitional, is thickened from t_c/β to t_c/β_s, where $\beta_s = t_c/[(t_c - t_{oc})/\beta + t_{oc}]$ (Fig. 3), by the addition of melt. This modifies the estimate of β obtained from seismic measurements of crustal thickness. Such measurements yield β_s which must then be converted to β for modelling. The fraction of melt available for segregation depends on the amount of incoming asthenosphere which is determined by β (Fig. 3). Proportionally smaller amounts segregate in regions where β is smaller, thereby giving a smooth transition from

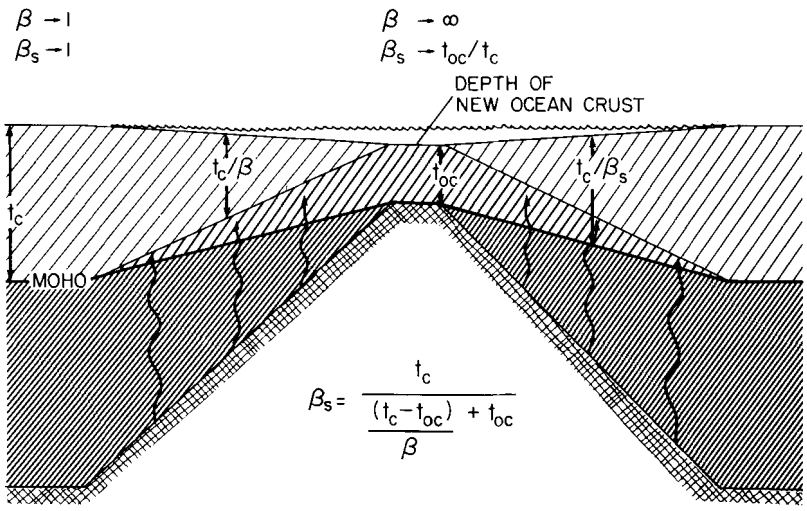

Figure 3. A two-dimensional cross-section showing how the uniform extension and melt segregation model produces oceanic crust and a smooth transition from unextended continental crust, $\beta = 1$, to oceanic crust, $\beta \to \infty$. The medium density shading illustrates the basaltic melt that thickens the crust in this region from t_c/β to t_c/β_s. The basaltic melt can equally well be considered to intrude the overlying extended crust. The amount of melt that segregates is proportional to the amount of incoming undepleted asthenosphere.

unextended continental crust through extended continental crust, with an added basaltic fraction, to oceanic crust.

The asymptotic thermal contraction subsidence for this model is,

$$S_C\,[\beta(x), t \to \infty] = \frac{\alpha T_m}{2 - \alpha T_m}\left\{a\left(1 - \frac{1}{\beta}\right) - S_I\right\}$$

and is the same as that for the uniform extension model.

2.3 THE DEPTH-DEPENDENT EXTENSION MODEL

It is unlikely that extension will be uniform with depth during rifting because the rheological properties of the lithosphere change rapidly with depth as evidenced by listric faulting (Montadert *et al.* 1979). The depth-dependent extension model (termed non-uniform extension by Sclater *et al.* 1980 and Royden & Keen 1980) approximates this inhomogeneous response to stress by assuming that the upper and lower lithosphere are decoupled at a depth d, corresponding to a detachment, or shear zone, at which listric faults in the overlying brittle zone sole out. The zone above d extends by an amount β while the zone beneath undergoes ductile extension by δ (Figs 1 and 2). (Note that the $\delta - \beta$ convention is reversed with respect to that of Royden & Keen 1980 and Sclater *et al.* 1980.)

Royden & Keen (1980) show that the initial subsidence predicted by the model is

$$S_I[\beta(x), t = 0^+] = \left\{a - \frac{(t_c - d)\rho_{c2av} - (a - t_c)\rho_{0av}}{\rho_0'}\right\}\left(1 - \frac{1}{\delta}\right)$$

$$+ d\left(\frac{1}{\delta} - \frac{1}{\beta}\right) - \frac{d\rho_{c1av}}{\rho_0'}\left(1 - \frac{1}{\beta}\right)$$

where,

$\rho_{c1av} = \rho_c(1 - \alpha T_{c1av})$,

the average density for $z < d$;

$\rho_{c2av} = \rho_c(1 - \alpha T_{c2av})$,

the average density for $d \leqslant z \leqslant t_c$;

$$T_{c1av} = \frac{T_m}{2}\frac{d}{a},$$

the average temperature for $z < d$;

$$T_{c2av} = \frac{T_m}{2}\left(\frac{d}{a} + \frac{t_c}{a}\right),$$

the average temperature for $d \leqslant z \leqslant t_c$.

The corresponding asymptotic thermal contraction subsidence is

$$S_C[\beta(x), t \to \infty] = \frac{(a - S_I)\,\alpha(T_{iav} - T_{fav})}{1 - \alpha T_{fav}},$$

where

$$T_{iav} = \frac{1}{a - S_I}\left\{\frac{d}{\beta}\frac{T_m}{2}\frac{d}{a} + \frac{(a-d)}{\delta}\frac{T_m}{2}\left(1 + \frac{d}{a}\right) + \left(a - S_I - \frac{d}{\beta} - \frac{(a-d)}{\delta}\right)T_m\right\},$$

$$T_{fav} = \frac{T_m}{2},$$

which gives

$$S_C = \frac{\alpha T_m}{2 - \alpha T_m}\left\{\left(a - \frac{1}{\delta}\right) - S_I + d\left(\frac{1}{\beta} - \frac{1}{\delta}\right)\left(2 - \frac{d}{a}\right)\right\}.$$

For large δ and small β values this model predicts initial uplift when $d \approx t_c$ (Royden & Keen 1980, fig. 6) unlike the previous models. This uplift occurs on extension, unlike that which develops in response to horizontal heat flux which requires time to grow (Appendix A).

As noted by Royden & Keen (1980) choosing $\delta \neq \beta$ produces space problems, but $\delta > \beta$ can be accommodated by allowing magmatic intrusion into the brittle region or by proposing that the extended lower zone originally occupied a smaller horizontal interval $x' < x_0$ (Fig. 1). The model is also limited by the difficulty of estimating δ because lithospheric thinning is not preserved on cooling. However, the model is compelling in that doming is a feature of contemporary rift systems and there is evidence for a wide zone of attenuated lithosphere beneath their flanks, corresponding to $\delta > \beta$ (Brown & Girdler 1980; Panza, Mueller & Calcagnile 1982; Fairhead & Reeves 1977; King & Williams 1976). It remains to be determined whether uplift and significant extension occur simultaneously or whether one precedes the other (King & Williams 1976).

3 The thermo-mechanical model

The coupled thermo-mechanical model traces the evolution of a rifted margin as it cools, contracts and is loaded by sediment and water. The first-order thermal aspects of this

evolution have been discussed by McKenzie (1978), Royden *et al.* (1980), Keen (1979), Royden & Keen (1980) and Watts & Steckler (1979). The results show that subsidence should be proportional to $(\text{time})^{1/2}$ for approximately one lithospheric thermal time constant and then trend to an exponentially decaying form. All these authors assumed a local model of isostatic equilibrium. This may be approximately correct for hot extended regions soon after rifting, but is increasingly in error in later stages of evolution when the cooling and thickening lithosphere becomes stronger and exhibits significant bending or flexural characteristics. The thermo-mechanical model includes both the thermal aspects of the evolution and their isostatic (mechanical) consequences.

3.1 THE THERMAL MODEL

The thermal model is based on interpolations between one-dimensional finite difference solutions for the conductive cooling and thickening of a self-contracting subsiding lithosphere as a function of changing β (and δ) with position across the margin. This form implicitly ignores lateral heat flux, but considers first- and most second-order effects in the vertical, z, direction to ensure accurate solutions for mass and temperature distributions. This is particularly important because the gravity anomalies calculated from the results are very sensitive to mass distribution.

The one-dimensional equation of heat transport in the absence of radioactive heat generation is

$$\frac{\partial}{\partial z}\left[K(t)\,\frac{\partial T}{\partial z}\right] = \rho c\left(\frac{\partial T}{\partial t} + v_z\,\frac{\partial T}{\partial z}\right)$$

where T = temperature, K = thermal conductivity, ρ = density and c = specific heat; $\kappa = K/\rho c$ = thermal diffusivity. The last term is the contribution of advection to the local change in thermal energy due to subsidence of the lithosphere at velocity v_z which can be estimated from the anticipated rate of isostatic subsidence under water and sediment loads. This term includes only the physical displacement of the whole lithosphere in response to surface loads and does not include the effects of downward movements due to self-contraction. Its main effect is to transport hot material through the base of the model.

The initial temperature distribution $T(z, \beta, t = 0^+)$ is that predicted by the rifting models of Section 2 and Appendix B. The upper boundary, normally at the seafloor is maintained at $T = 0°\text{C}$, while the bottom boundary ($z = 0$) remains at $T = T_m$ to limit the maximum lithospheric thickness to 'a', the value before extension. This is only an approximation to a bottom melting condition because no latent heat of fusion or density change is associated with the boundary, although they could be included (Parker & Oldenburg 1973). The condition does, however, ensure that material advected through the base of the model is at near solidus temperatures and, therefore, that the energy flux is minimized.

The model has two regions, sediments ($K = K_s$, $\rho = \rho_s$, $c = c_s$, etc.), and lithosphere–asthenosphere ($K = K_0$, $\rho = \rho_0$, $c = c_0$, etc.), and heat flux is continuous at the interface. Crust is considered to have the same thermal properties as the rest of the lithosphere. The sediments, which are deposited at 0°C, are conductively heated. The effects of thermal blanketing due to the deposition of the low conductivity sediments is included in the equations. The sediments are assumed to have thermal properties equal to the mean, suitably calculated, for the whole sediment column at that location.

Addition of sediment modifies the position of the upper boundary of the thermal model in a manner predicted by the mechanical model. It should also be noted that heat can be lost by advection through the upper boundary when there is uplift that results in erosion. This

enhances conductive cooling by increasing the near surface thermal gradient. The converse, thermal blanketing, is of course true in regions that receive sediments.

The equations were reduced to a first-order finite difference set on a uniform spatial grid stepsize Δz, time stepsize Δt, and were solved by Gaussian elimination for finite increments in time ($\Delta t^j, j = 1, n$) the thermo-mechanical timesteps and as a function of position across the margin. During each of the thermo-mechanical timesteps the model properties were held constant, therefore many Δts(~ 0.1 Ma) elapse during each Δt^j(~ 10–20 Ma). At the end of each Δt^j boundary, interface and isotherm positions, thermal and density parameters, sediment thickness and subsidence velocity, are updated as a result of predictions of the mechanical model.

The thermal contraction subsidence, ΔS_C^j for each of the n model timesteps is calculated from the change in model thickness during the jth timestep on the assumption of a uniform volume coefficient of thermal expansion, α,

$$\Delta S_C^j = \alpha \left\{ \int_{z=0}^{u^j} T^j(z)\, dz - \int_{z=0}^{u^{j-1}} T^{j-1}(z)\, dz \right\},$$

where u^j is the position of the upper boundary during the model timestep. The integral is evaluated numerically for each Δz, using the trapezoidal rule, and subsidence is accumulated upwards from the bottom, $z = 0$, to yield the total subsidence of the surface, ΔS_C^l. The updated model is then regridded on to the uniform Δz, Δt finite difference grid for the next model timestep.

It is important to ensure that second-order effects due to self-contraction within the model are included, so that energy is conserved. Otherwise significant errors result in the gravity calculations. At each level, z, in the model the grid size, Δz, decreases on cooling and self-contraction by $\alpha \Delta T(z)$, where $\Delta T(z)$ is the change in temperature for each model timestep. This increases the subsidence by a factor $[1 + \alpha \Delta T(z)]$ at that level.

3.2 THE MECHANICAL MODEL

Fig. 4 illustrates the way in which changes in the flexural properties of the lithosphere have been included in the model. The depth to a particular isotherm, here called the relaxation isotherm, T_R, is determined from the thermal model after self-contraction at the end of each model timestep. This depth is used to define the thickness of an elastic plate whose mechanical response to loading is then determined. This model is similar to the flexure of a uniform elastic plate that has previously been used (e.g. Watts & Ryan 1976), but differs from this simpler flexural model in that its thickness will vary both with time as the lithosphere cools, and with position across the margins.

The relaxation isotherm cannot be specified in an *a priori* way although results from studies of olivine micro-rheology (Beaumont 1979) and of the isostatic response of oceanic lithosphere to various loads (e.g. Watts 1978), suggest that $450°C \leqslant T_R \leqslant 750°C$. Therefore, T_R is considered to be a variable to be determined from comparison of model results with observations. A further complication, addressed in more detail later, is that an incompetent brittle upper crustal layer may be created by faulting during rifting (Fig. 4). Therefore, the rheological lithosphere, which is the part of the thermal lithosphere which undergoes flexure, should be strictly defined as the region below the brittle layer and above the relaxation isotherm; in this paper it initially is defined as the region below the sediments and above T_R. This is partly compensated by choosing lower values of T_R than indicated above and is discussed in more detail later, as is the basis for this type of mechanical model.

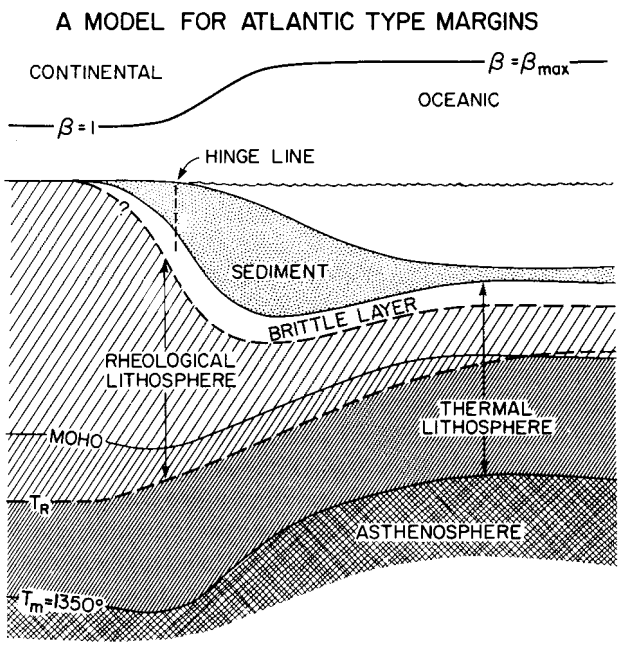

Figure 4. The mechanical model showing the distribution of $\beta(x)$; the brittle crustal layer, faulted during extension; the rheological lithosphere, that region which responds elastically to sediment and water loads; the thermal lithosphere, that region from the base of the sediments to the melting isotherm, T_m; and the crust and asthenosphere. Note that the region below the relaxation isotherm, T_R, is assumed to act as an inviscid fluid which buoys up the rheological lithosphere.

A two-dimensional elastic finite element model (Bathe, Wilson & Iding 1974) is used for the mechanical calculations (Fig. 5). The four noded isoparametric elements include the complete stress and strain tensors, and no simplifications of the type implied by 'thin' or 'thick' plate theory were assumed. The boundary conditions are: the upper surface is a free surface subject to vertical nodal loads; lateral far field boundaries are no slip, and are at a

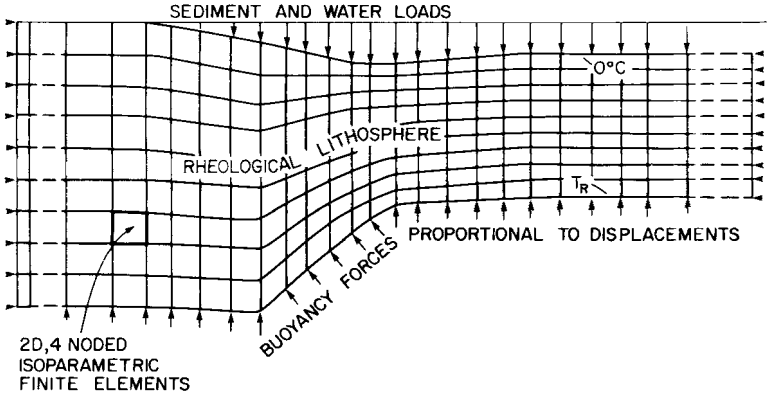

Figure 5. Simplified version of the finite element mesh used in the mechanical model. The mesh of 9×46 elastic elements is uniform in size with depth, z, at any location, but has a gradation in the horizontal, x, direction. The smallest elements in the extended zone have $\Delta x \sim 12$ km, whereas those near the boundaries have $\Delta x \sim 500$ km. The elements all have the same material properties. Poisson's ratio, $\nu = 0.25$; Young's modulus, $E = 2 \times 10^{11}$ Pa.

distance greater than ten flexural wavelengths from the margin; and the bottom boundary is free but subject to normal tractions. These basal tractions, needed to simulate buoyancy from an underlying fluid density ρ_f, are included by modifying the global stiffness matrix to allow for forces proportional to vertical displacement of the basal nodes. The material properties of the plate are uniform linear elasticity with Young's modulus ($E = 2 \times 10^{11}$ Pa) and Poisson's ratio ($\nu = 0.25$). ρ_f was set equal to $\rho_0(1 - \alpha T_m)$ to simulate underlying asthenosphere. The grid has nine equi-depth elements in the vertical direction and 46 horizontal elements distributed such that the nodes are approximately 12 km apart on the margin but grade to > 500 km in the far field. Model tests confirmed that these boundaries do not influence the solution in the region of interest. The finite element grid must be reformulated for each model timestep to reflect the change in shape and thickness of the region between the base of the water and sediments and the relaxation isotherm. The same lateral node distribution is used in each reformulation.

Water and sediment loads are considered piecewise linear between nodes and are converted to nodal loads to reflect this distribution. There are two methods of sediment loading. The 'palaeo-bathymetry method' adds sediments and water until a desired configuration for their interface is achieved. In this way specified slopes, or depths, for the shelf, rise, and abyssal parts of the model can be achieved. The 'thickness method' adds a specified thickness of sediment which can vary in a piecewise linear manner across the model. Water is then added to sea-level. The thickness method was used in this paper.

It is readily appreciated that in neither case can the correct thickness of water and/or sediment which will fill the basin be selected in an *a priori* manner. This is because isostatic adjustments will influence the sediment configuration. An iterative loading approach is used whereby finite element solutions are repeated with sequentially updated loads that reflect the approach to equilibrium (see Beaumont 1978). To speed this convergence a 'first guess' is used in which it is assumed that the loads are those predicted by local isostatic equilibrium. The model is judged to have converged when changes in the overall load are less than 1 per cent.

Flexurally or thermally uplifted crust and sediment that are exposed above sea-level are iteratively eroded until equilibrium is achieved. A record of the sediment, crust and water distribution must be kept in order that eroded material can be unloaded from the model with the correct density.

The results of the converged iterations are then used to update the model stratigraphy, water depth and positions of the Moho and isotherms. These updated variables are then used to reformulate the finite difference thermal model for the next model timestep. The loads considered for each timestep are solely those appropriate for that timestep because each timestep can be treated as a discrete entity for a linearly elastic rheology.

It can be seen that the finite difference thermal and finite element mechanical models are separate yet coupled. Primary coupling is from thermal to mechanical properties through the position of the relaxation isotherm. Feedback from sediment blanketing and erosion modifies the cooling history, thermal contraction and tectonic subsidence. There are additional secondary interactions that have only small effects on the model configuration but must be included to ensure mass and heat conservation, themselves related through thermal expansion, and therefore, accurate gravity anomaly calculations.

3.3 JUSTIFICATION OF THE RHEOLOGICAL MODEL

The justification for modelling the mechanical behaviour of the lithosphere as described is based on evidence (see Weertman 1970; Ashby & Verall 1977; Beaumont 1979, for example)

that isostatically induced deviatoric stress, σ^D, within the lithosphere and asthenosphere but below the brittle zone, is relaxed through viscous flow such that the effective viscosity η follows a thermal activation law that can be approximated by

$$\eta = \eta_0 F\{\sigma^D\} \exp\left(-\frac{A' T_m}{T}\right)$$

where T/T_m is the homologous temperature, and A' is an activation energy. This simple Weertman law demonstrates that no matter whether $F\{\sigma^D\} = c\sigma^D$, giving a linear creep law, or $F\{\sigma^D\} = c'(\sigma^D)^n$, where $n \sim 3$–5, giving power-law creep, the effective viscosity is primarily an exponential function of temperature and that for a linear temperature gradient η will be an exponential function of depth. In cold, near surface regions η will be sufficiently large that no significant stress relaxation will occur over geological time-scales (< 10 Ma), whereas it is known that within the asthenosphere significant viscous flow occurs in glacio-isostatic rebound (Peltier 1974) for time-scales $\sim 10^{-2}$ Ma, reflecting a much lower effective viscosity. Between these regions there is a transition region whose depth depends on the temperature distribution and the time-scales under consideration. To a first approximation it is assumed that this region can be modelled as a single interface between an overlying elastic region and an underlying incompressible inviscid fluid region. The position of the interface is determined by the relaxation temperature, T_R. Surface loads are compensated by deformation of the elastic region, without stress relaxation, supported by the buoyancy of the underlying region in which stress is totally relaxed. This is obviously an approximation to the true variation of viscosity with depth but probably provides a sufficiently sensitive rheological model because viscosity changes by many orders of magnitude over a small temperature range. It implicitly assumes that, for continental margins, thickening of the elastic region during lithospheric cooling dominates tendencies for the effectively elastic region to become thinner by stress relaxation. Therefore, stresses become 'frozen in' whereas in other environments, where there is a stable thermal regime, apparent thinning of the elastic region during isostatic adjustment may reflect stress relaxation (Beaumont 1981).

The depth to the relaxation isotherm is a model parameter which is best interpreted as the depth at which stress relaxation becomes significant on time-scales of ~10 Ma. The elastic region is termed the rheological lithosphere to differentiate it from the thermal lithosphere, that region where temperatures are significantly below the solidus. There is no reason to expect the two lithospheres to have the same thickness because significant subsolidus creep occurs on time-scales much less than 10 Ma (Beaumont 1979).

3.4 SEDIMENT PROPERTIES AND COMPACTION

In this paper the physical properties of the sediment are considered to vary with time in a manner that depends primarily on their degree of compaction and depth of burial. Such variations were not considered by Keen *et al.* (1981). The model of sediment compaction is based on work by Sclater & Christie (1980) and Royden & Keen (1980). The sediment thickness available at the beginning of each model timestep was determined by decompaction of the appropriate part of the sediment section as presently observed, according to the simple porosity–burial depth relation (Rubey & Hubbert 1960),

$$\phi = \phi_0 \exp(-h d_z),$$

where ϕ is the porosity, d_z is the depth below the top of the sediments, and ϕ_0 and h are empirical constants which were determined for each of the major lithologies (Table 1) using sonic and density logs from exploratory wells. As more sediments are added, the porosity

and thickness of the deeper sediments decreases due to compaction. Densities are calculated on the assumption that sediments are formed of a matrix of grains, with densities ρ_{sg} peculiar to each sediment type, and water, of density ρ_w, that occupies voids made available by porosity. Thus,

$$\rho(z) = [\rho_w \phi_0 + \rho_{sg}(1 - \phi_0)] \exp(-hd_z).$$

The effects of overpressured regions in the sediment section off Nova Scotia are not considered in this paper; the basic method for decompaction as described by Sclater & Christie (1980) was used.

Sediment compaction does not cause first-order changes to model predictions of basement position because dewatering transfers mass from the sediments to the water column, thereby preserving the overall load. However, second-order effects that determine the space available for sediments and changes in density with depth are important. Corrections to sediment compaction, densities and model stratigraphy are made for each iteration of the mechanical model. Compaction is also regarded as an irreversible process, therefore no decompaction occurs in regions which are unloaded in response to erosion.

The thermal conductivities of each sediment column are also adjusted at the end of the mechanical iterations to reflect changes in porosity and overall composition. Each basic sediment type was assigned a thermal conductivity based on published measurements on rock samples (Table 1). Changes in conductivity due to porosity or to mixing of two or more sediment types were then computed using the Maxwell model (Beck 1976). The weighted mean of the thermal conductivities in the sediment column is used as the sediment conductivity in the thermal calculations.

3.5 MODEL TESTS

A number of tests were used to assess the accuracy of the thermo-mechanical model and to set parameters for the numerical calculations in order to obtain an overall accuracy of 1 per cent. A comparison of vacuum loaded models, without self-contraction, with analytical solutions (McKenzie 1978) demonstrated that suitable choices for Δz and Δt, the finite difference increments, were 0.5 km and 0.1 Ma. Mechanical models that had a uniformly thick elastic layer gave sufficiently accurate results with the same number of elements as shown in Fig. 5, when compared with the flexure of uniform beams. Such models also predict the correct local isostatic balance for longer wavelength loads.

The accuracy of the asymptotic solutions for vacuum, water and sediment loads were confirmed by considering an 11 timestep model spanning 350 Ma (> 5 model thermal time constants) for which 99.6 per cent of the potential subsidence has been achieved. That there were a sufficient number of model timesteps was also confirmed by varying the lengths of those timesteps. This suggests that the model is relatively insensitive to the discrete nature of sedimentation and model updating.

The best evidence that the model is accurate, when the full range of complexities is included, is that the predicted gravity anomalies appear accurate.

3.6 A SUMMARY OF THE COMPUTATIONAL METHODS

For each of the models in this paper the required input variables are: (1) the variation in $\beta(x)$ and $\delta(x)$, (2) the value of T_R, (3) the values of the thermal, mechanical and sedimentological parameters, and (4) the sediment budget. Calculations are then performed

by stepping the models through time in model timesteps usually chosen to be 10–20 Ma. The procedure is as follows:

(1) At $t = 0$, extension occurs resulting in the initial subsidence as predicted by local isostatic adjustment. This depression is then filled with a combination of sediment and water to simulate loading of the continental margin just after formation. Isostatic adjustment to this load is calculated using the mechanical model described above.

(2) A time interval, Δt^j elapses during which the lithosphere cools and subsides as predicted by the thermal model; the position of the isotherm T_R also changes and a further load of water and sediment accumulates. Isostatic adjustment is again calculated by the mechanical model, adjusted for the new depth of T_R.

(3) This process is continued over the number of timesteps necessary to simulate the evolution of the margin. After each timestep, the depths to the seafloor and to the basement, the position of the Mono discontinuity and the gravity anomaly across the margin are computed.

4 Gravity calculations

For each model timestep the thermo-mechanical model predicts the shape and density distribution of each of the following bodies: (1) seawater, (2) sediments, (3) continental and oceanic crust, (4) the mantle component of the lithosphere and, (5) the asthenosphere. Within the sediments, lithosphere, and asthenosphere, the density also varies with temperature according to $\rho = \rho_0 (1 - \alpha T)$ where ρ_0 is the density at 0°C, α is the volume coefficient of thermal expansion and T is the temperature excess over 0°C. A comparison of the free air gravity anomalies arising from this mass distribution with those observed for typical, and specific, margin transects provides a powerful constraint on the state of isostatic balance at continental margins because the gravity anomalies are a sensitive function of the relaxation isotherm.

Before describing the methods of gravity calculation it is important to emphasize that all results were determined entirely from the input variables described in the last section; $\beta(x)$; T_R and the sediment budget. No arbitrary adjustment of the configuration of the basin or of crustal structure were made to force the results to resemble any observational data. In this manner, the validity of the conceptual model can be properly assessed. This is particularly important in interpreting the gravity anomalies across rifted margins; often somewhat arbitrary models are presented which are justified solely on the fit of the model's gravity anomaly to the observations. Given the non-uniqueness of gravity modelling techniques, such results may not be meaningful. In the present case, however, agreement between predicted and observed gravity anomalies provides a powerful constraint on acceptable models. It is our opinion that gravity calculations are of limited value except when used to test the validity of dynamical models that are based on as few input variables as possible.

The gravity anomalies were calculated using analytical expressions for the first derivative of the gravitational potential for homogeneous two-dimensional polygons (Okabe 1979). The divergence theorem is used to reduce two-dimensional volume integrals to line integrals around a contour defined by straight line segments enclosing material whose density can be considered uniform. This is a particularly suitable form because the model calculations provide densities and interface positions defined in a piecewise linear form on a non-uniform grid. The method also avoids problems with singularities and provides accurate results for external points, and points on the contour. An algorithm automatically sorts the model results for region of equal density, describes the contours and calculates the total contributions for an array of field points.

The calculations were separated into two parts, an evaluation of the anomalies on the assumption that model densities assumed their 0°C values and a perturbation that occurs by virtue of density changes on heating to the predicted temperature distribution. The reference model for these calculations is that before extension. The results are presented as contributions from three components: (1) the sedimentary basin, including water and sediments, assumed to be at 0°C, and termed the 'basin anomaly'; (2) perturbations arising from changes in the position of the model Mohorovičić discontinuity from its reference position, termed the 'Moho anomaly'; and (3) the overall thermal perturbation from the reference state, termed the 'thermal anomaly'. The size of the individual component anomalies can be much larger (~ 500 mgal) than their sum, the free air gravity anomaly ($\lesssim$100 mgal), and it is instructive to see how they individually change and compete against each other as the model evolves.

The practice of separating a component of the gravity anomaly that is purely the result of thermal perturbations is useful because it shows how large, particularly in the early stages of evolution, the thermal contribution can be, and explains the necessity for lateral variations in mantle density used in conventional models of continental margins. Also, because the overall free air gravity anomaly arises from such disparate sources, it is unlikely that a particularly meaningful interpretation could be given to the isostatic response function (the wavenumber domain transfer function between bathymetry and observed gravity anomaly) for such an inhomogeneous system.

The calculated gravity anomalies proved to be one of the best tests of the correct isostatic and mass balance for the model because they are sensitive to both the rifting process and later thermo-mechanical evolution. A correct mass-to-heat balance as determined by thermal expansion was especially important; errors as small as 10 m in predicted thermal contraction subsidence, S_C, led to errors of ~ 2 mgal in the gravity anomalies. The most stringent test was that the far field free air anomaly ($x \to \pm\infty$) $\to 0$. A tolerance of ±2.5 mgal was allowed in this, acknowledging third-order errors in the isostatic balance that resulted from, among others, the bottom boundary condition. That the three component anomalies also tend to their 'uniform Bouguer slab' limits as $x \to \pm\infty$ is another useful test.

5 The Nova Scotian margin

Rather than present results for a series of typical continental margin cross-sections, an attempt is made to model the development of what we believe to be the best studied mature Atlantic-type margin, that off Nova Scotia. Previous work (Jansa & Wade 1975; Barrett & Keen 1976) has shown that the margin underwent rifting between 200 and 180 Ma ago. It is presently the site of a large syn- and post-rift sedimentary wedge whose stratigraphy beneath the shelf region is relatively well known from exploratory drilling (Figs 6 and 7) (Jansa & Wade 1975; Barss, Bujak & Williams 1979; McIver 1972; Given 1977). At greater depths and further offshore, the stratigraphy can be inferred from multi-channel seismic reflection data and correlated to the well sections. The depth of the deepest parts of the basin has been estimated from seismic refraction measurements along strike with the margin, as has the variation in crustal thickness in the transition from continent to ocean (Keen *et al.* 1975; Keen & Hyndman 1979; Keen & Cordsen 1981; Dainty *et al.* 1966).

Gravity data, density and sonic logs, as well as sediment lithologies and bottom hole temperatures from the wells, and evidence on thermal metamorphism of the sediments are also available (Robbins & Rhodehamel 1976; Purcell, Rashid & Hardy 1979; Lewis & Hyndman 1976; Hyndman *et al.* 1979; Bujak, Barss & Williams 1977a, b; Shih, MacNab & Halliday 1981). These data provide estimates of the necessary input variables for the model as previously described. They also provide tests for comparison with the model predictions.

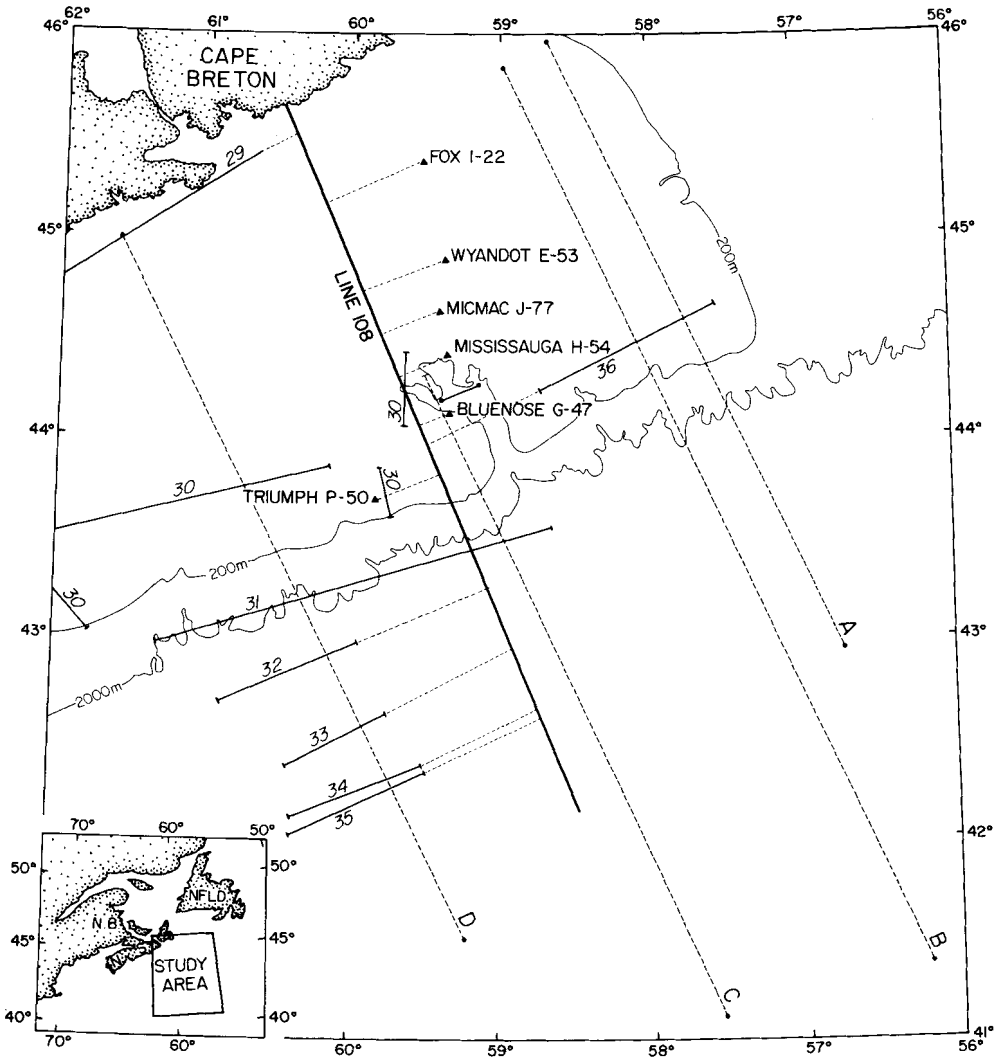

Figure 6. Location map of the sources of data used in this study. The heavy solid line is the line of the cross-section (shown in Figs 7 and 9); it is also the location of seismic reflection line 108. The triangles are deep exploratory wells. The dashed lines are the tracks along which free air gravity anomalies used in this paper (Fig. 18) have been measured. Solid lines show the positions of deep crustal seismic refraction lines. The numbers associated with these refer to the publications in which the results are described: 29–30, Dainty *et al.* (1966); 31–34, Keen *et al.* (1975); 35–36, Keen & Cordsen (1981). The well data and the refraction data have been projected on to line 108, as shown by the fine dashed lines.

The relationships between the thermal and seismic data have already been discussed by Keen (1979), Hyndman & Keen (1979) and Royden & Keen (1980). Royden & Keen (1980) estimated $\beta(x)$ from the subsidence histories of individual wells and compared the results with refraction data for crustal thickness for the transect shown in Fig. 6. This transect is again considered in this paper however, only forward modelling of the basin development given a $\beta(x)$ distribution is considered. Keen (1979) and Watts & Steckler (1979) have also studied individual wells and produced convincing arguments for thermally controlled subsidence of the shelf region seaward of the hinge line. Fig. 7 represents a regional compilation of the most up-to-date non-proprietary data for this section. No attempt has been

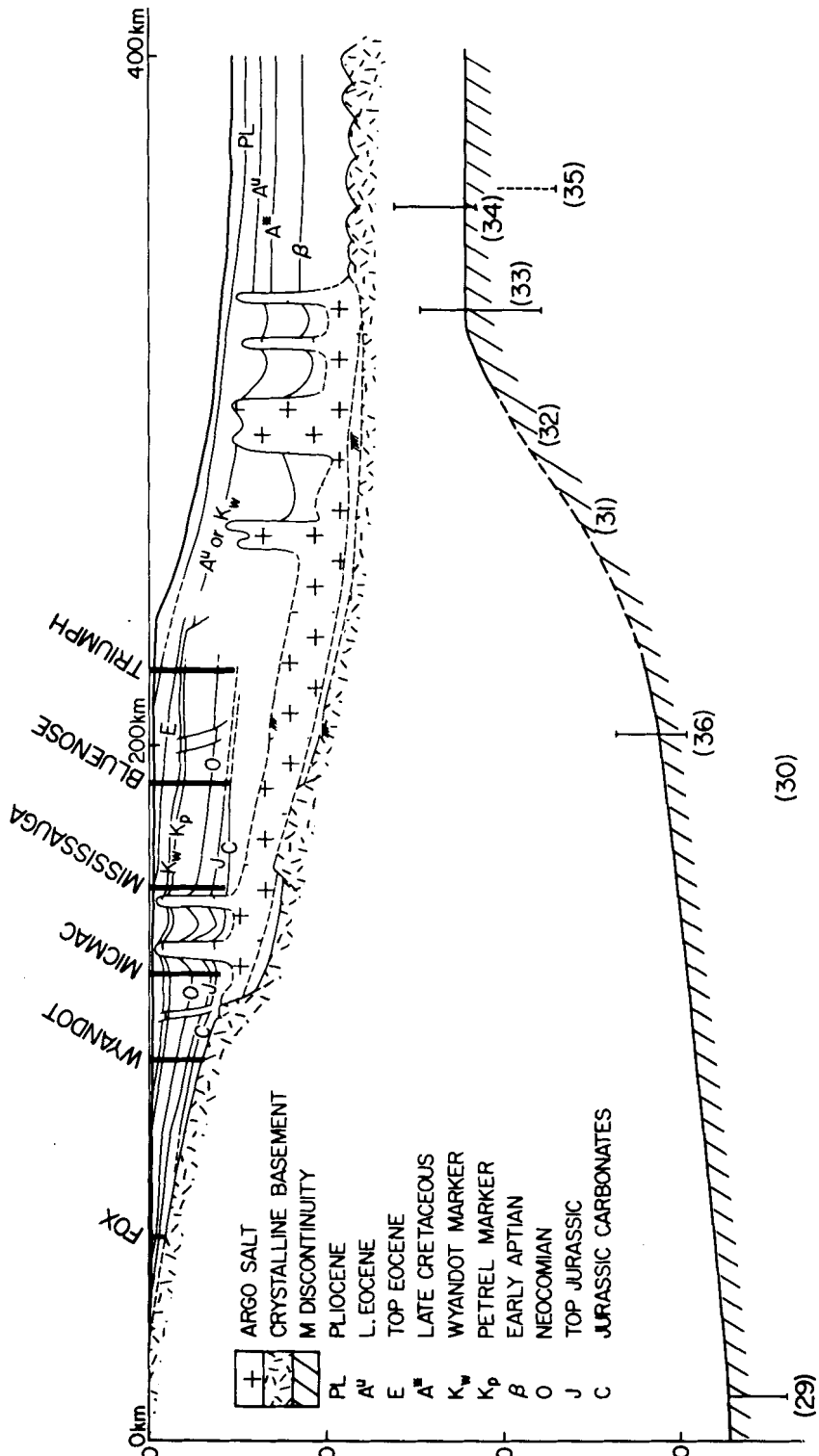

Figure 7. Composite cross-section of the Scotian Basin and crust along the line shown in Fig. 6. The depth to the Moho at the ends of the seismic refraction lines (Fig. 6) is shown as the vertical bars which are thought to represent the variability of crustal structure along strike. The refraction lines are labelled in the same manner as those in Fig. 6. Regions where the positions of interfaces remain somewhat uncertain are shown as dashed lines. The position of the basement–sediment interface beneath the basin is specified on the basis of wells that intersect it (Fox and Wyandot), seismic reflection and seismic refraction (shown by //////) observations. This basement is thought to be that of syn- and post-rift sediments; older sediments may extend to greater depth. Stratigraphy of the basin is based on evidence from deep exploratory wells (shown as vertical bars) and seismic reflection data (Jansa & Wade 1975; and Wade 1981 private communication). Lithologies are regional averages representing the dominant component. Where unshaded, the sediments are mainly clastics (see text for additional details).

made to include any observed features that have a small spatial scale ($\lesssim 10$ km), or that are not well established by the data. Where interpolations were necessary, in the basement depth for example, these are shown as dashed lines. No attempt has been made to restore the section to a state prior to extensive diapirism in the two salt provinces. Basedment and other seismically identified time-stratigraphic events are poorly located in these regions. Identifications of seismic reflectors are based on Jansa & Wade (1975) and Wade (1981, private communication) and the appropriate chrono- and lithostratigraphic correlation chart is given (Fig. 9). The reflectors are inevitably diachronous to some degree. Neither do they necessarily correspond with the stratigraphic horizons of the models shown later which were chosen to coincide with period and stage boundaries on the basis of biostratigraphic and absolute age data from Van Hinte (1976a, b) for the Mesozoic, and Berggren (1972) for the Cenozoic. A further interpretation of the observations (Fig. 9) yields a general stratigraphic and lithological cross-section with inferred stratigraphic horizons that are isochrons and correspond to the same ages as those of the models. This is the section that was decompacted to obtain sediment thickness and lithology necessary as inputs to the model. More detailed information on observed and predicted present age–depth relations and lithologies for selected wells and on predicted subsidence histories is given in the results section.

6 Model results

The results presented are those from a series of models in which selected model parameters were systematically varied to illustrate the sensitivity of the results to these parameters. Preliminary modelling (Keen *et al.* 1981, 1982) established that $T_R = 250°C$ gave the best agreement with observed free air gravity anomalies. Therefore, the first three results follow the evolution of $T_R = 250°C$ models for differing rifting mechanisms. The results establish whether details of the rifting process can be estimated from a study of mature margins. The second series of results illustrate the sensitivity of the depth-dependent extension model to variations in T_R. The intention is to place bounds on acceptable values of T_R. In the last two models the effects of crustal and sediment radioactive heat generation, and a brittle near surface lithospheric layer are investigated.

In all models the sediment budget, sediment properties, model densities and thermal properties are identical. All models follow the 'thickness method' of sedimentary filling, one criterion of success or failure being the ability of the model to accommodate the prescribed sediment distribution and yet maintain the correct palaeobathymetry. The results are particularly sensitive to erosion of overfilled regions, where sediment extends above sea-level, which in turn leads to sedimentary layers that are ultimately too thin.

The $\beta(x)$ distribution was estimated from the observed crustal thickness (Fig. 7) on the assumption that the crust had a uniform thickness, $t_c = 35$ km, before extension. This is the present crustal thickness measured at the landward end of the profile (Fig. 6) beyond the margin of the basin. Trial values of $\beta(x)$ were varied within these constraints in order to obtain the best agreement with observed basin structure. In the case of the melt segregation model the seismic refraction observations of crustal thickness provide $\beta_s(x)$ which is then converted to β using $t_c = 35$ km and $t_{0c} = 6.5$ km.

6.1 UNIFORM EXTENSION MODEL, $T_R = 250°C$

The evolution of basin stratigraphy and free air gravity anomaly at six stages is shown together with the β distribution in Fig. 8. In total there were 11 timesteps at 0, 10, 25, 41, 50, 64, 85, 104, 125, 152, 185 Ma after rifting with time intervals chosen to be short during

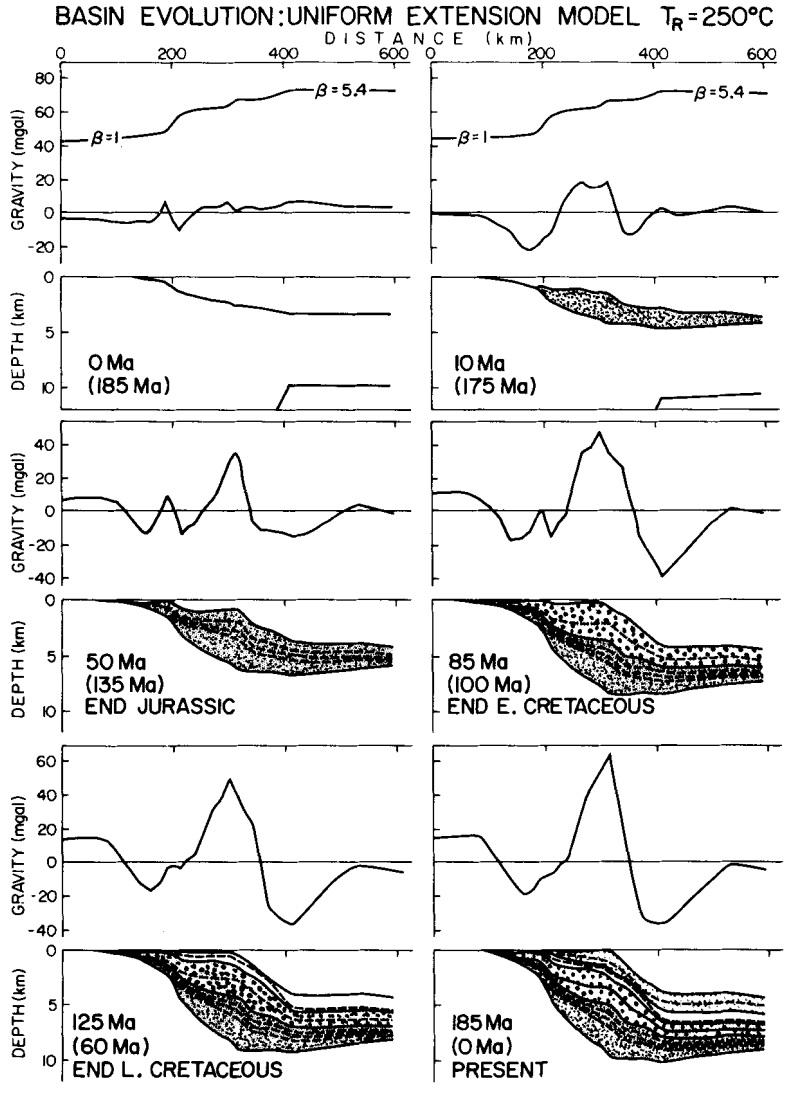

Figure 8. The evolution of the sedimentary basin and gravity anomalies for the uniform extension rift model with relaxation isotherm, T_R = 250°C. The top panel in each column shows the distribution of the extension, graphed as $[1-1/\beta(x)]$, with β_{max} = 5.4 used to represent oceanic crust by thinned continental crust. The times without brackets are the elapsed times since rifting, whereas those in brackets are the age. The solid lines are stratigraphic horizons corresponding to basement, the end of the Jurassic, the end of Lower Cretaceous, the end of the Upper Cretaceous and the present sediment–water interface. Dashed lines are those for the other timesteps with post-rifted elapsed times of 10, 25, 41, 64, 104 and 152 Ma. The gravity anomalies are the predicted free air anomalies.

rapid evolution but longer after most of the thermal contraction had occurred. The lithospheric thermal time constant is 62.8 Ma. Some timesteps were also chosen to coincide approximately with stage and period boundaries and four of the six intervals shown correspond to the end of the Jurassic (135 Ma), Lower Cretaceous (100 Ma), Upper Cretaceous (60 Ma) and Quaternary (0 Ma) periods. The stratigraphic boundaries corresponding to these periods are shown as solid lines in the figures, whereas those for the remaining timesteps are

dashed. The final basin stratigraphy is also shown in greater detail in Fig. 10 and should be compared with Fig. 9, the input stratigraphy.

The general pattern of sedimentation and the basin configuration is in good agreement with observations. For example, Tertiary and younger sediments are confined to points seaward of the inner shelf and there is an overall decrease in rate of sedimentation up the stratigraphic column. Very little sediment was truncated by erosion suggesting that subsidence of the model was closely in agreement with the true subsidence rate. However, pre-Cretaceous subsidence rates may have been too rapid leaving what are apparently excessive shelf water depths of up to 1 km. For times later than 64 Ma after rifting the palaeowater depths are in reasonable agreement with those observed when eustatic sea-level variations, which are not modelled, are taken into account. The early pattern of sedimentation in the shallowest part of the basin landward of the MicMac well is also unacceptable, a significant depression remaining in the sediment until the end of the Jurassic. Also, subsidence of this region immediately follows rifting suggesting that the oldest sediments on pre-rift basement should be ~ 185 Ma in age and not ~ 155 Ma as observed in the wells.

The evolution of the gravity anomalies reflects both the increasing depth of the basin and the increasing strength of the lithosphere. The pattern of a major high flanked by two lows is established soon after rifting, but it is only at 185 Ma that the amplitudes become similar to those observed.

The change in component contributions to the gravity anomalies from rifting to 185 Ma (Fig. 11) demonstrates the importance of the thermal gravity anomaly and the magnitude of each of the individual components. The evolutionary decay in the thermal component is compensated by a negative shift in the basin and Moho components. Significant features of the final free air anomaly (Fig. 8) are almost totally attributable to the oscillations in the basin component, $150\,\text{km} < x < 350\,\text{km}$. The main features of plots of the gravity components for all the models were similar; minor differences in the basin and Moho contributions reflecting differences in the degree of local isostatic equilibrium, and differences in initial thermal contributions which are attributable to the rifting models.

The thermal evolution (Fig. 12) illustrates the decay of the initially high thermal gradient in the 'oceanic' region which was simulated by extended continental crust with the same thickness as oceanic crust, $\beta = \beta_{max} = 5.4$. The base of the lithosphere is the $T = T_m = 1350^\circ\text{C}$ isotherm shown in the first panel. The other panels correspond to the same stages of evolution as those of Fig. 8 and show that the thermal anomaly has almost totally decayed. The figures also show the conductive heating of the sediments. The present maximum predicted temperature of the deepest sediments below the edge of the shelf and upper slope is $\sim 130^\circ\text{C}$. Increased thermal gradients in the sediments with respect to the lithosphere occur because the sediments have a lower thermal conductivity. A temperature of $\sim 75^\circ\text{C}$ is achieved in the deepest sediments at the end of the Jurassic when a significantly enhanced thermal gradient remained in the extended region. Thermal anomalies predicted by this model are a minimum because the rifting model does not generate oceanic crust and lithosphere at $T = T_m$. A detailed comparison of basin and temperature evolutions of this and other models is presented later.

6.2 COMPARISON OF RESULTS FOR DIFFERING RIFTING MECHANISMS

Results corresponding to those of Figs 8 and 12 for the uniform extension model are shown for all three rifting models in Figs 13, 14 and 15. Only three stages (0, 50 and 185 Ma) were chosen for comparison because the results converged rapidly. Model parameters were chosen so that the crustal thicknesses following rifting were the same although generated by differing processes. The δ distribution for the depth-dependent extension model was chosen to

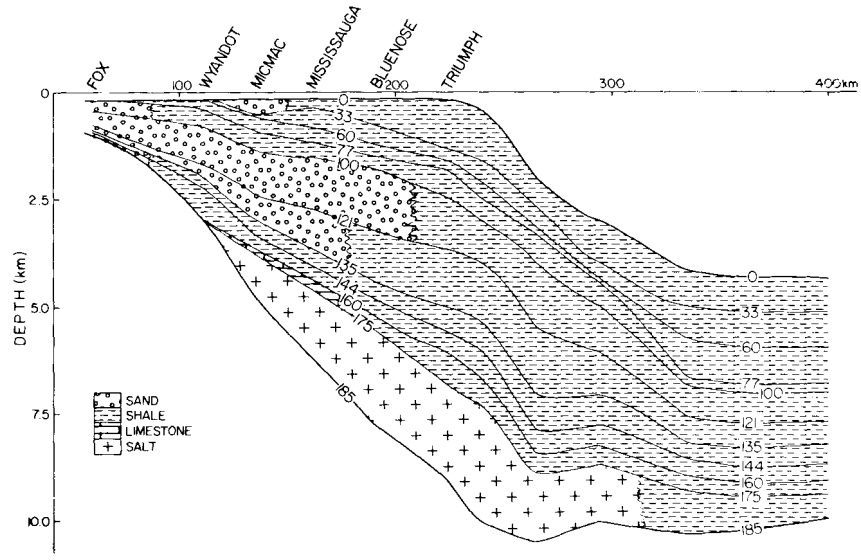

Figure 9. Generalized and interpreted chrono- and lithostratigraphy of the Scotian Basin along the section of Fig. 6. This interpretation of the section shown in Fig. 7 has a chrono-stratigraphy that was also used in the theoretical models (e.g. Fig. 10). The correlation chart (after Jansa & Wade 1975) illustrates the relationship between the seismic stratigraphy and the interpreted section. The section is also restored to remove the effects of diapirism. The lithology has been simplified to include the four components shown. In the cross-section only the dominant sediment type in an area for a given time interval is shown; however, the calculations allowed for mixtures of two components and such mixtures were used. This is the section that was decompacted (Section 3.4) and used as the sediment budget for the theoretical models.

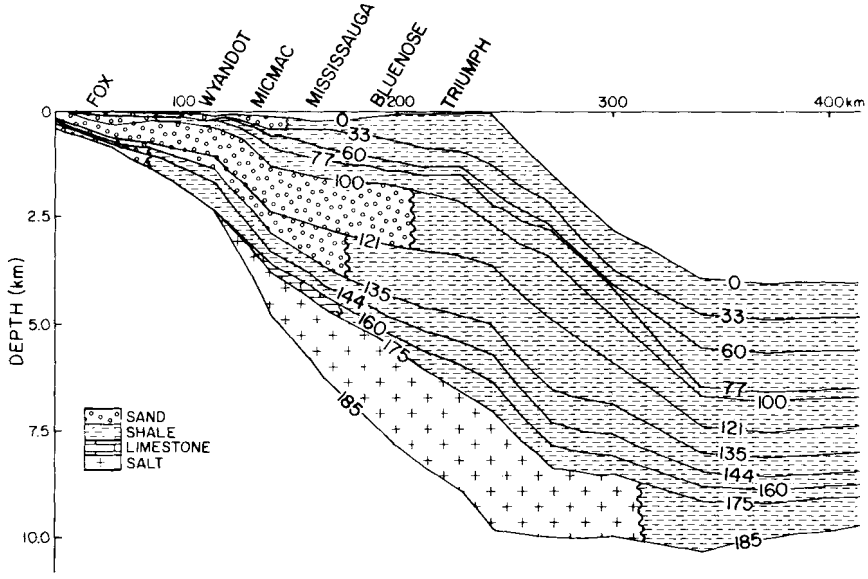

Figure 10. Stratigraphy of the uniform extension, T_R = 250°C, model basin (Fig. 8) 185 Ma after rifting for comparison with Fig. 9. Good agreement exists between the observed and computed strata, suggesting an underlying validity to the model.

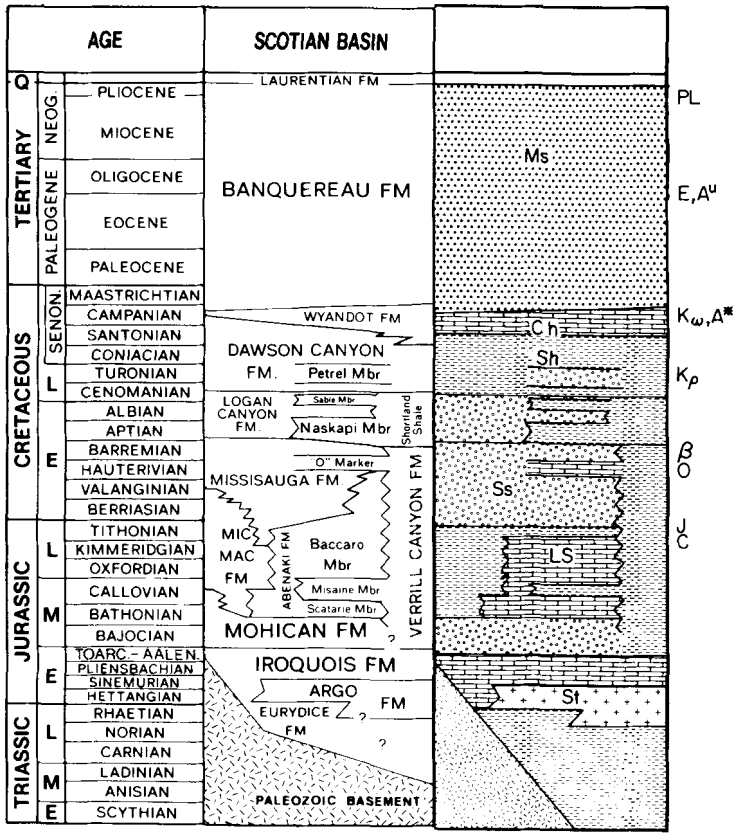

Figure 9 – *continued*

maximize the difference from the uniform extension model and yet predict a final stratigraphy in agreement with observations. The decoupling depth d was chosen equal to t_c, the initial thickness of the crust.

The differences among the models, where they exist, mainly result from differences in water loaded initial subsidence, which are greatest in the oceanic region, 2628, 3305 and 2923 m respectively for melt segregation, uniform extension and depth-dependent extension models (Fig. 13). Both the uniform extension and melt segregation models predict only subsidence, with the latter predicting less subsidence in the continental slope region as a consequence of the more realistic model for the ocean–continent transition. However, early subsidence of this region is not well constrained by observational evidence and the differences cannot be tested. These two models are almost identical landward of the shelf edge, both suffer from the same problem of early sedimentation landward of the MicMac well as mentioned previously. This problem is addressed by the depth-dependent extension model which predicts initial uplift of up to 420 m for this inner shelf region by virtue of the large values of δ (Fig. 13), thereby preventing sedimentation immediately after rifting. A net uplift remains even under the tendency of seaward loads to cause flexural downwarp. The particular version of this model shown does not allow erosion of the uplifted region, and therefore, sedimentation cannot occur until the region subsides below sea-level in response to the combined effects of thermal contraction and flexure. The oldest post-rift sediments predicted for the Wyandot and Fox wells, ~159 Ma, are in reasonably good agreement with

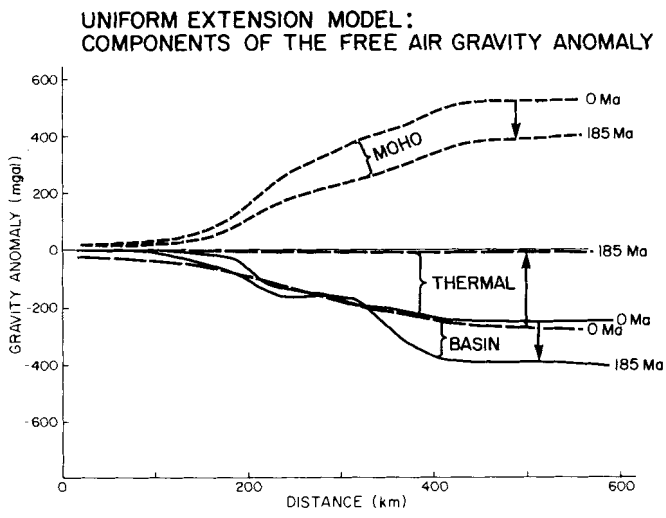

Figure 11. Components of the predicted free air gravity anomaly for the uniform extension, T_R = 250°C, model (Fig. 8) at 0 and 185 Ma after rifting. The Moho and basin components are those arising from the crust, and sedimentary basin and water, respectively. The thermal gravity anomaly, which decays with time after rifting, is that part of the gravity anomaly due to thermal expansion of the model in excess of its initial state, as is explained in the text, Section 4. The arrows indicate the direction of the evolution of these components.

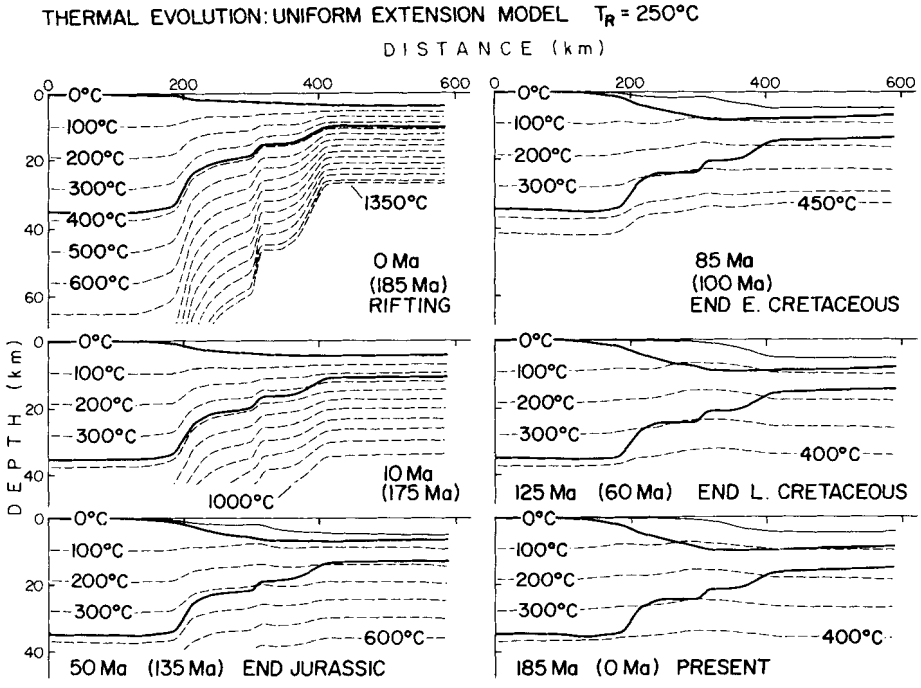

Figure 12. Thermal evolution of the uniform extension, T_R = 250°C model. Isotherms are shown as dashed lines and are contoured at 100°C intervals. The bold lines are the sediment–basement interface and the Moho. Times without brackets are post-rift elasped times; those with brackets are ages. The panels correspond to those of Fig. 8.

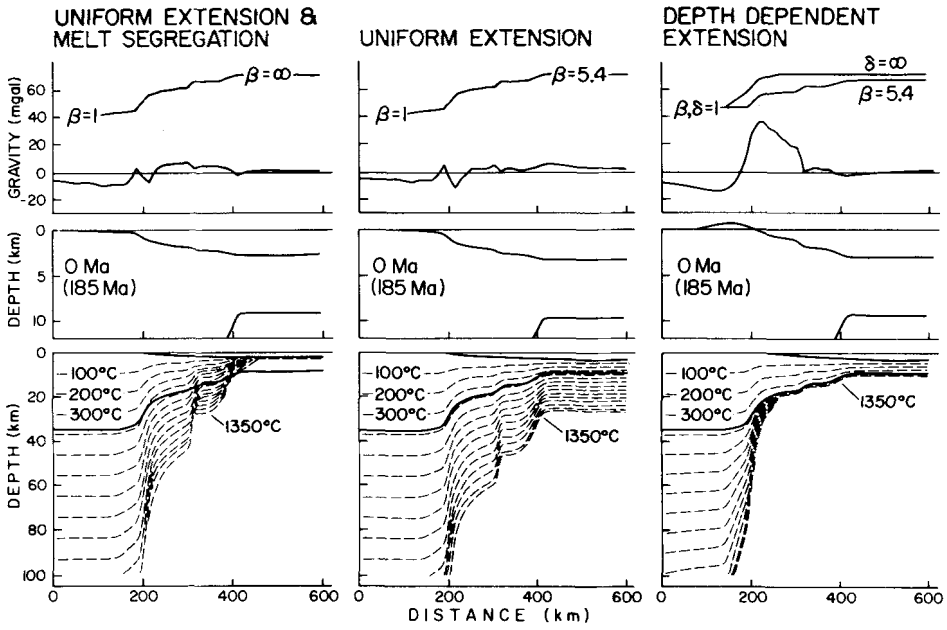

Figure 13. Comparison of model results on rifting, T_R = 250°C, for the three rifting processes. The panels shows the β and δ distributions (graphed as $1-1/\beta$ and $1-1/\delta$), the free air gravity anomalies, a crustal cross-section, and distribution of isotherms. Note that the depth-dependent extension rifting model results are significantly different from the others.

observations, ~162 and $\gtrsim$155 Ma. This is the maximum delay for the chosen $\beta(x)$ and $\delta(x)$ because substantial erosion would give earlier sedimentation. Eustatic sea-level changes, not modelled, would also influence sedimentation though only through perturbations to the overall pattern.

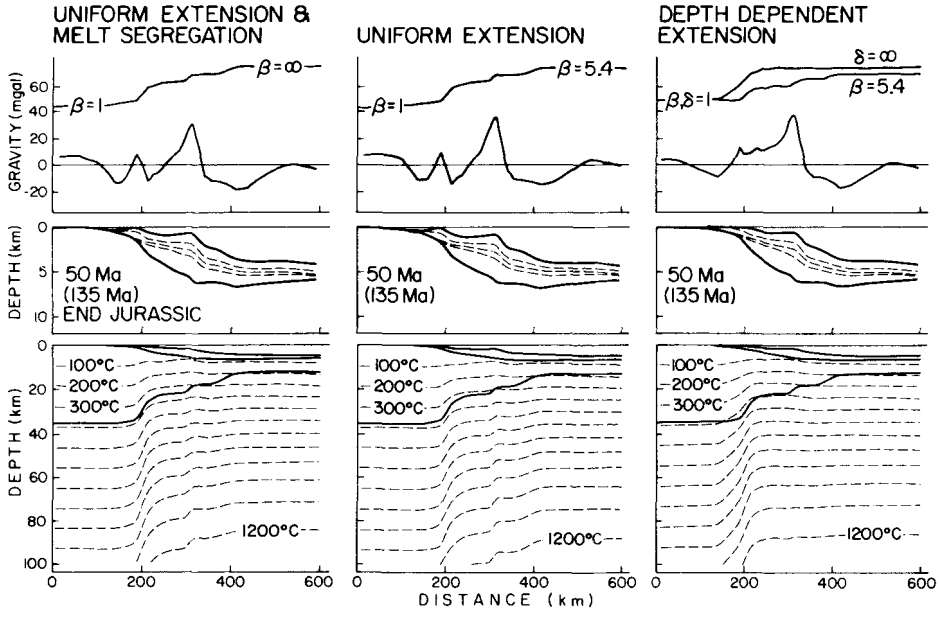

Figure 14. Results corresponding to those shown in Fig. 13 but at 50 Ma after rifting.

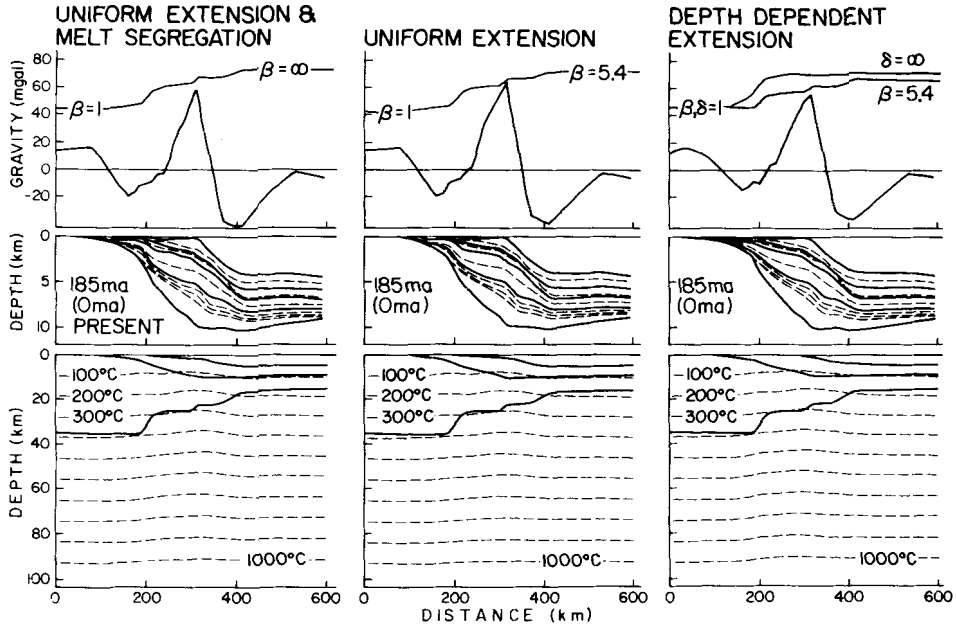

Figure 15. Results corresponding to those shown in Figs 13 and 14 but at 185 Ma after rifting.

The depth-dependent extension model also predicts what is believed to be a more realistic early shallow pattern of sedimentation. Sediment deposited for the first 10 Ma is believed to be mainly salt and, where sampled, this is known to have been deposited in shallow water (Jansa, Bujak & Williams 1980 and Wade, private communication). This does not, however, provide compelling evidence in favour of the depth-dependent model, because shallow water salt could have been deposited in any of the rifting models if the rifting process was coeval with the salt deposition, spanned a period $\gtrsim$10 Ma, and deposition kept pace with subsidence. The precipitous initial subsidence is an artifact of the model which assumes instantaneous rifting.

The gravity anomalies of the depth-dependent extension model are significantly different from those of the other two models for the first 50 Ma after rifting. However, the decay of thermal differences between the models leads to gravity anomalies at 185 Ma that are indistinguishable. Additional differences in the evolutions of the models are also almost imperceptible leaving only minor differences in stratigraphy as a possible key to the rifting process.

These results are disappointing in one respect. They indicate that, as suggested by simple scaling arguments, it is unlikely that the details of differing rifting mechanism can be detected from studies of mature margins unless the basin stratigraphy is very well known. Conversely, studies of subsidence history, evolution of gravity anomalies and thermal maturation are shown to be relatively insensitive to the details of the rifting process. An estimate of $\beta(x)$ is, therefore, all that is necessary for a first-order thermo-mechanical model for a mature margin. This result is only as expected. The margins have a fading memory of their thermal origins. The memory is significant for approximately one lithospheric thermal time constant.

6.3 THE DEPENDENCE OF MODEL RESULTS ON THE CHOICE OF RELAXATION ISOTHERM

Examination of the dependence of model results on the choice of T_R = 0, 250 or 450°C demonstrates that the gravity anomalies are probably the most sensitive indicator of the

state of isostatic balance at continental margins. In Fig. 16 basin stratigraphy and free air gravity anomalies for 185 Ma old depth-dependent extension models are compared. The values of $\beta(x)$ and $\delta(x)$ are the same as those of previous models. Fig. 17 illustrates the corresponding change in thickness of the rheological lithosphere from $T = 0$ to 185 Ma as a function of relaxation isotherm. The effect of an increasingly thicker rheological lithosphere is to distribute the isostatic response to loading over increasingly longer wavelengths while maintaining the same overall response as measured by the cross-sectional area of the basin. $T_R = 0°C$ corresponds to local (or Airy) isostasy, consequently the extent of the basin is limited to regions where $\beta > 1 (x > 130\,\text{km})$, that is regions where crustal extension has

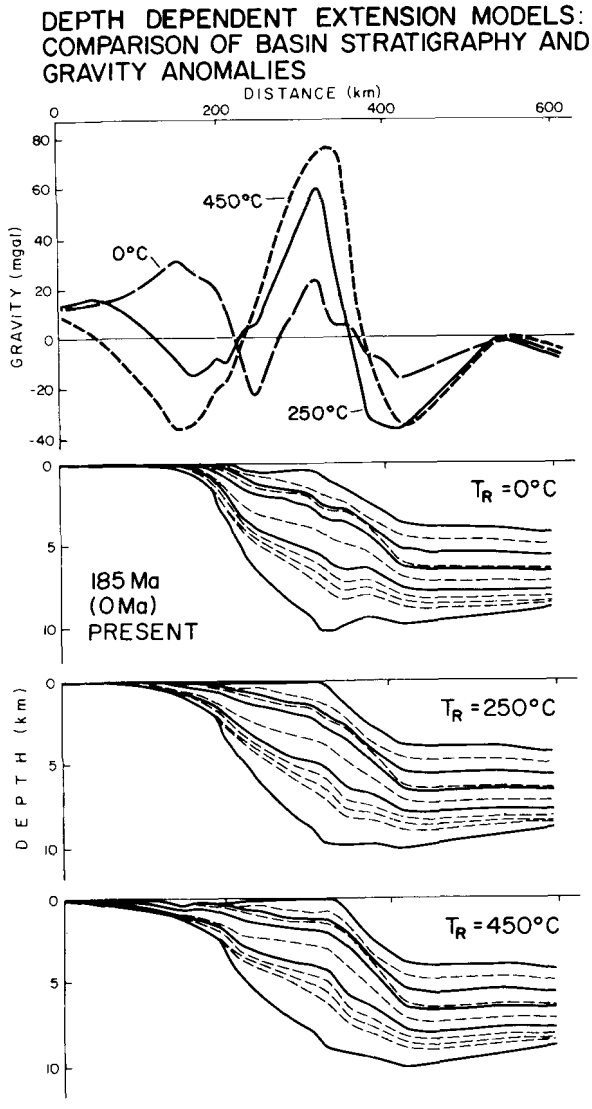

Figure 16. Comparison of free air gravity anomalies and basin stratigraphy of depth-dependent extension models ($d = t_c$, and β and δ as shown in Figs 13 14 and 15) at 185 Ma after rifting. The differences reflect variations in the choice of relaxation isotherm; T_R = 0, 250 and 450°C. Note the significant difference of the 'Airy' model, T_R = 0°C, and the increase in amplitude of the anomalies with increasing T_R.

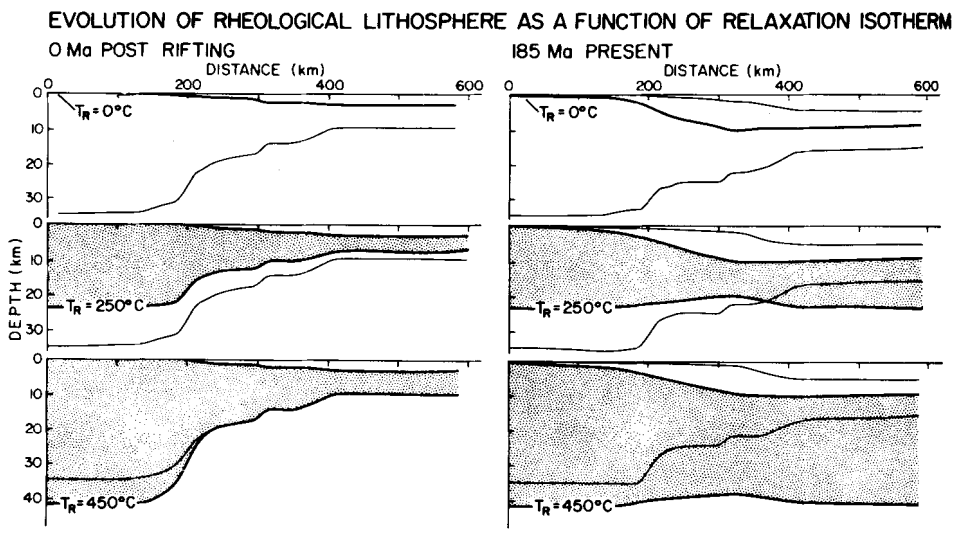

Figure 17. Evolution of the rheological lithosphere (stippled) from rifting to 185 Ma for depth-dependent rifting models ($d = t_c$, and β and δ as shown in Figs 13, 14 and 15) as a function of increasing relaxation isotherm. The fine lines show the position of the sediment–basement interface and the Moho.

occurred. For finite T_R, loads induce a downward flexure of the lithosphere landward of this point. Even further inland the flexure changes sign giving rise to an upwarped peripheral crustal bulge which may be eroded. Similarly flexed regions occur seaward of the foot of the model continental slope but these are less prominent because they are smoothed by loading of overlying oceanic sediments and there is, of course, no erosion. The down-flexed regions are balanced by a reduction in the maximum depth of the basin beneath the shelf edge, by comparison with the $T_R = 0°C$ model. Flexure also progrades the deepest point in the basin toward the foot of the continental slope. The magnitude of these effects depends on the choice of the isotherm and the amount of flexural coupling between oceanic and continental lithosphere. Sediment that loads the thinned margins soon after rifting causes more localized flexure than corresponding loads on a mature margin because the extended lithosphere is initially less rigid, but thickens and becomes more strongly coupled to the unextended continental lithosphere with time (Fig. 17).

It can be seen from Fig. 16 that $T_R = 0$ and 450°C result in underfilled and overfilled sedimentary basins. The resulting progradation of the shelf break in the $T_R = 450°C$ model is particularly noticeable. Similarly, these values of T_R lead to underestimates and overestimates of sediment extent landward of the hinge line, that point at $x \sim 190$ km seaward of which the basin rapidly deepens. The hinge line is interpreted as marking the transition between the flexurally and thermally induced region of the sedimentary basin. Patterns of subsidence differ on either side of this boundary.

The general trend in the gravity anomalies (Fig. 16) is that the larger the value of T_R, the larger the anomalies, a result that reflects the ability of a flexed plate to balance local mass excess against a neighbouring deficit (Fig. 17). Significant gravity lows correspond to mass deficits in downflexed regions where lower density sediments and crust respectively replace crust and mantle. Large gravity highs reflect the converse. The 10–15 mgal high landward of the basin at $x \gtrsim 40$ km is mainly due to the Moho, all significant long-wavelength thermal gravity anomalies having decayed (see Fig. 11).

Comparison of the $T_R = 250°C$ free air gravity anomaly with observations (see profiles A–D, Fig. 18) suggests that this is the best choice for T_R. Small ($\lesssim 15$ mgal), short-wave-

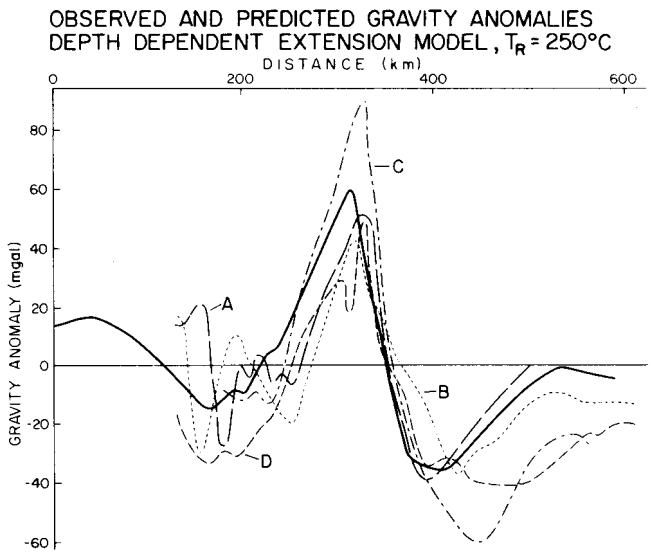

Figure 18. Comparison of observed free air gravity anomalies (from tracks A–D, Fig. 6) with that predicted by the depth-dependent extension model, T_R = 250°C, of Fig. 17, heavy solid line.

length oscillations in the observed anomalies probably reflect local density variations in the crust, or small undulations in the basin boundaries that were not modelled. Our intention is not to model every feature of the observed gravity anomalies, but to provide a dynamical explanation of the major trends. We must accept a background of residual (~15 mgal) anomalies which probably represent a measure of the Earth's failure to conform to the ideas of simple continuum mechanics.

7 Models that include radiogenic heat production

The models discussed in previous sections did not include any component of heat flux from radiogenic heat production in the crust or sediments. Such heat production is likely to modify the temperature distribution and, therefore, have a primary effect on the development of the margin through the position of the relaxation isotherm and on the temperature history of the sediments. A model for rifting in which a near surface layer of uniform heat production existed in the continental crust prior to rifting and depth-dependent extension occurs is discussed in Appendix B. Crustal heat production makes only minor modifications to the initial subsidence, whereas sedimentary heat production has a significant effect during the thermal contraction phase of basin development, as is shown in Fig. 19. The radioactive heat production rate within the model sediments depends on the lithology and is based on production rates for the sediment types listed in Table 1 (Hamza & Beck 1975; T. Lewis 1981, private communication) averaged within the sediment column for each model time-step in a similar manner to the other thermal properties. Crustal heat production was assumed to be the same as the average measured in surface rocks in Nova Scotia (Hyndman *et al.* 1979) and be confined to a surface layer 7.5 km thick prior to extension. The distribution of this layer after extension is shown in the upper panel of Fig. 19. Comparison of the predicted temperature distribution 185 Ma after rifting for depth-dependent extension models that differ only in radioactive heat generation demonstrates that the major effect is to increase substantially the near surface thermal gradient. A secondary effect is to thin the

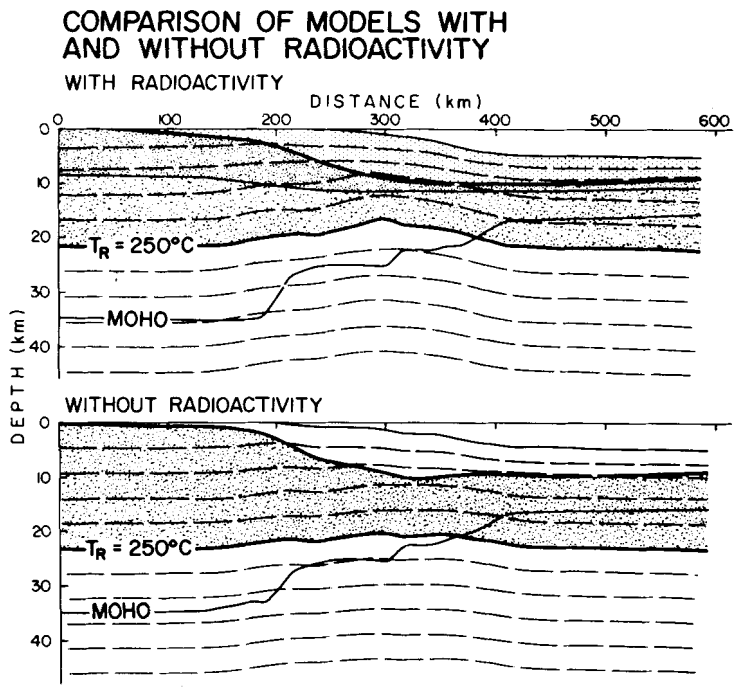

Figure 19. Comparison of depth dependent extension models, $T_R = 250°C$ ($d = t_c$, and β and δ as shown in Figs 13, 14 and 15) at 185 Ma after rifting with and without radioactivity. Temperatures are contoured at 50°C intervals. Sediments in the upper panel have radiogenic heat production based on values given in Table 1. The stippled areas show the rheological lithosphere which is noticeably thinned beneath the basin. The thin solid line with the crust in the upper panel shows the base of the thinned crusted layer of uniform heat production (see Table 1) which had a pre-rift thickness of 7.5 km.

rheological lithosphere ($T_R = 250°C$) particularly beneath the deepest part of the basin, but also beneath the oceanic part of the model. This thinning occurs throughout the evolution of the model and leads to a closer approach to local isostatic equilibrium beneath the shelf and slope regions than would otherwise have occurred. Despite this, the final basin is marginally shallower than the model without radioactivity because average temperatures are higher, thereby reducing the net thermal contraction subsidence. The gravity anomalies for both models are similar in character, although that for the model with radioactivity has a final peak to peak range that is approximately 10 mgal smaller than that for the model without radioactivity. This is apparently the result of a closer approach to local isostatic equilibrium.

8 An alternate model of the rheological lithosphere

The possibility of a near surface brittle layer of the lithosphere has been mentioned in the sections on depth-dependent extension and the thermo-mechanical model. Its existence, however, has not been explicitly included in the previous thermo-mechanical models, the rheological lithosphere having been defined as that region between the base of the sediments and the relaxation isotherm. The models, therefore, assumed that the fractured, brittle crustal region of thickness d/β, where $d = 35$ km, that existed after rifting was still capable of bearing stresses due to isostatic loading by sediments and water. If, however, this region

remains a passive broken unit that yields to applied stress by additional motion on pre-existing faults, the rheological lithosphere must be redefined as the zone between the base of the brittle layer and the relaxation isotherm. To achieve sufficiently large flexural properties for this redefined rheological lithosphere a larger value of T_R is necessary. It should also be noted that in this interpretation the base of the brittle layer corresponds to an isotherm immediately before and after rifting and that this isotherm, T_{BD}, can be considered to be that separating regions of brittle and ductile deformation.

Choosing $T_{BD} = 200°C$ and $T_R = 450°C$ in a depth-dependent extension model with $d = 35$ km gives results that are almost the same as the earlier ones for $T_R = 250°C$. This demonstrates that no unique value can be assigned to the relaxation isotherm, equal results being given for $T_R = 250$ and 450°C depending on the model. That a brittle listric faulted layer is known to be created in many examples of lithospheric extension (Hamilton & Myers 1966; Proffett 1977; Eaton 1979; Montadert *et al.* 1979) augurs in favour of $T_R > 250°C$ for the Nova Scotian margin. If the depth d were known from independent evidence T_{BD} could be specified and T_R determined by adjusting the model to give the best fit to observed gravity anomalies as before.

The reason $d = 35$ km was chosen for the earlier models was to maximize the effect of depth-dependent extension on the tectonic subsidence history. If we are now to interpret the upper layer explicitly as that corresponding with that known to have listric faults and to include this in the mechanical model, d must be reduced. It is assumed for the purposes of illustration that $d = 17$ km (i.e. $\sim t_c/2$) corresponding to $T_{BD} = 200°C$, a depth approximately equal to the maximum depth of continental crust earthquakes in extensional environments and an upper bound for the depth of the sole for listric faulting in the Basin and Range Province (Eaton 1979) and the Amorican margin of the Bay of Biscay (Montadert *et al.* 1979; Le Pichon & Sibuet 1982). Thus, the same value for the brittle–ductile transition depth is used in both the model of depth-dependent extension and in the thermo-mechanical model. The model results (Fig. 20) differ from those of Figs 14, 15, 16 and 19 because $d = 17$ km, not 35 km, $T_R = 450°C$, and radioactivity and the brittle layer are included. The structure of the basin is similar to that of the earlier depth-dependent extension models. It has the same maximum depth and a similar position for the shelf break. That the shelf edge is somewhat more rounded than earlier models reduces the peak amplitude and pointed nature of the associated gravity maximum. Sedimentation landward of the hinge line starts too early, like that in the uniform extension models, reflecting the lack of early uplift. Maximum temperatures of ~180°C beneath the shelf edge are ~20°C hotter than those predicted by any other model. This result was somewhat unexpected because the temperature gradient in the crust following rifting was lower than that for models where $d = 35$ km (Figs 17 and 20). However, this is partially offset by the thicker radiogenic layer that remains in the extended region as a result of lower values of β than in the previous models. The gravity anomalies are similar to, but smaller than, those of previous depth-dependent extension models. They remain very subdued, $\leqslant \pm 20$ mgal, for the first lithospheric thermal time constant and at no point exceed a range of 80 mgal. The reasons for this are evident from Fig. 20 which shows that in the early stages of evolution, when sedimentation rates are greatest, the rheological lithosphere is very thin beneath most of the basin giving local isostatic equilibrium and small gravity anomalies. It is only later, when sedimentation has slowed, that the rheological lithosphere achieves a significant thickness beneath the oceanic region. Even then the oceanic and continental regions are partially decoupled by the combined effects of upwarping of the isotherms by sedimentary blanketing and downwarping of the brittle–ductile interface by sediment loading. With this in mind, it is not surprising that the mature margins remain zones of weakness even though they occupy

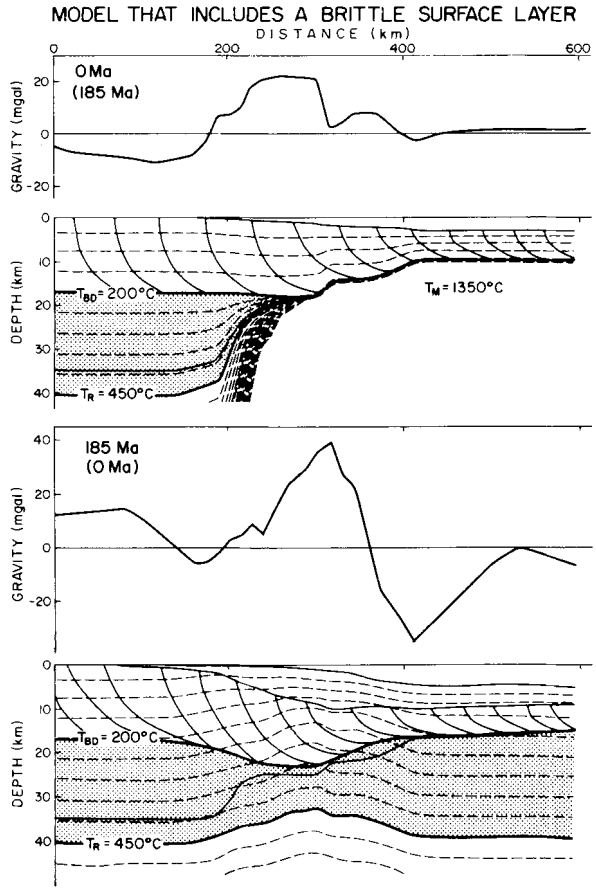

Figure 20. Free air gravity anomaly and cross-section of a depth-dependent extension model, which includes a brittle layer, at 0 and 185 Ma after rifting (T_R = 450°C, t_c = 35 km, d = 17 km, T_{BD} = 200°C, radiogenic heat production as in Fig. 19). Isotherms are contoured at 50°C intervals. The brittle region is shown pervaded by listric normal faults created during rifting. The stippled region represents the rheological lithosphere. Note the thinning of the rheological lithosphere beneath the basin even at 185 Ma.

an intraplate position. Compressional reactivation would seem to be comparatively easy for heavily sedimented margins, whereas a starved margin should appear somewhat stronger. The similarity of the overall results with previous ones suggest that it will be difficult to define correctly the rheological lithosphere without additional independent evidence on T_{BD} and T_R and their stress dependence.

9 Age–depth relations and subsidence histories for individual wells

In the same way that the cross-sections give an idea of the broad-scale features of the model results, age–depth curves from individual exploratory wells illustrate the model capabilities on a finer scale (Fig. 21). They compare unmodified observations based on biostratigraphic data from Barss *et al.* (1979) for the wells shown in Fig. 7 with model predictions. It is important to emphasize that the age–depth curves plot sediment age as a function of depth at a particular time. They are not subsidence curves, which trace the history of a particular

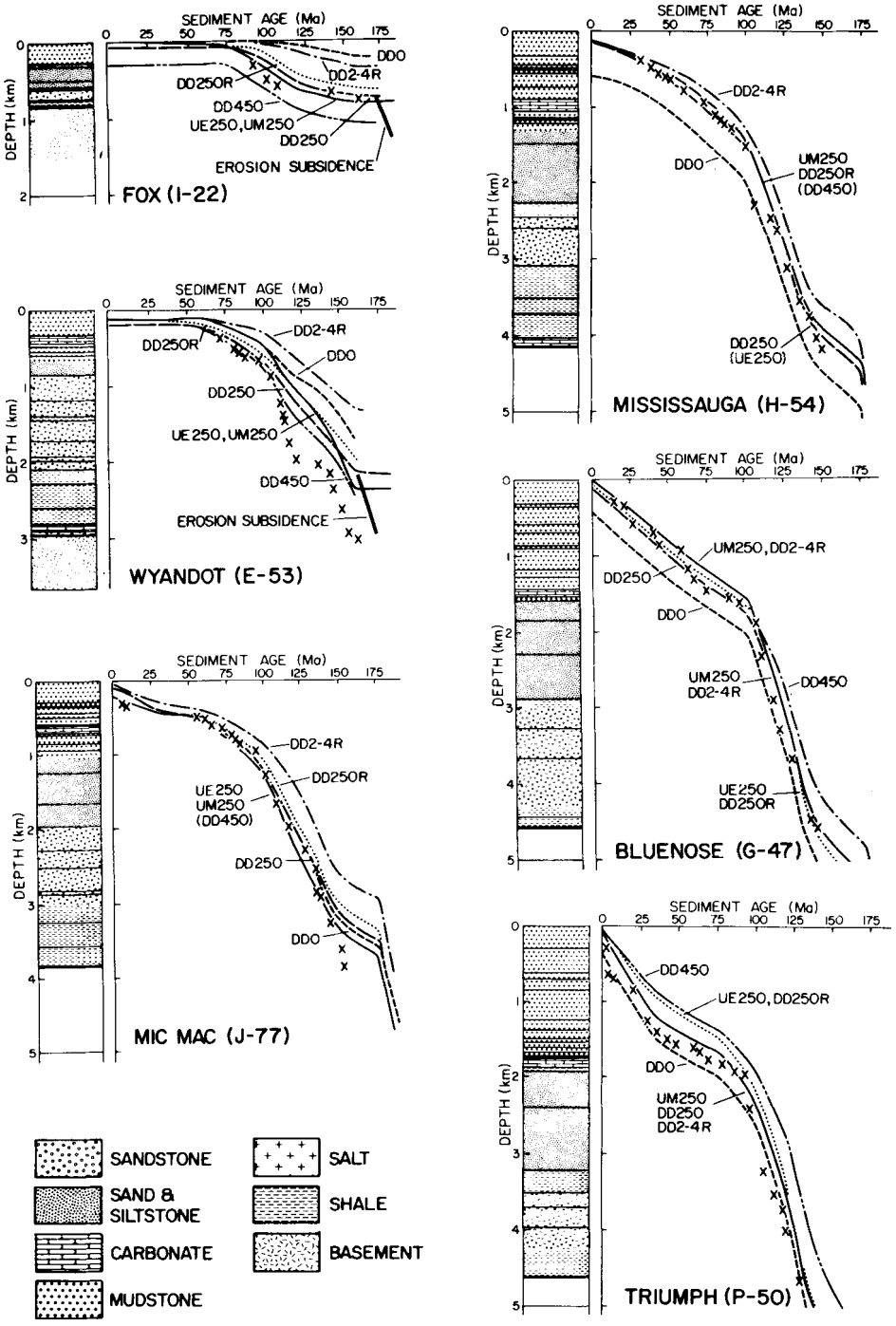

Figure 21. Currently observed and predicted age–depth relationships for the deep exploratory wells shown in Figs 6 and 7. Generalized lithologies from the wells are also shown. The ×'s are the observations and the continuous, dashed, and dotted lines are theoretical results from the models. The first two letters of the labels indicate the rifting model (UE = uniform extension, UM = uniform extension and melt segregation, DD = depth-dependent extension). The numbers are the values of the relaxation isotherm, e.g. '250' means T_R = 250°C. '2–4' is the model with the brittle crustal layer with T_{BD} = 200°C and T_R = 450°C. An 'R' means that the model included sedimentary and crustal radioactive heat generation. Curves that have more than one label indicate that those models gave results that were almost the same within the resolution possible in the figure. A label in brackets indicates that his model gave a similar subsidence curve which has been omitted to reduce confusion. The bold lines labelled 'erosion subsidence' indicate the maximum possible additional sedimentation, had uplifted crustal regions of the depth dependent models been instantaneously eroded (see text for further details).

point, nor can the observations be converted to tectonic subsidence curves without interpretative calculations that are subject to some uncertainties. For example, backstripping assuming local isostatic equilibrium is subject to error. The figures illustrate whether the models correctly predict the present age–depth relations; the tectonic subsidence is then easily obtained from the models, as are the effects of regional isostatic adjustments. The models do not, however, include the effects of eustatic sea-level change, therefore some deviation of the observations from the predictions is anticipated. For this reason it also appeared unrealistic to include a comparison of observed and predicted palaeobathymetry. Eustatic sea-level changes are easily included in the models and will be included in future detailed studies.

The results (Fig. 21) demonstrate the generally good agreement between observations (crosses) and theory (continuous and dashed lines) for all wells except Wyandot. Theoretical results are labelled 'UE' (uniform extension), 'UM' (uniform extension and melt segregation), and 'DD' (depth-dependent extension); the following number, e.g. '250', refers to the temperature in °C used for the relaxation isotherm ('2–4' is the model including the surface brittle layer and using T_{BD} = 200°C and T_R = 450°C), and an R implies that the model had a radioactive layer. For the sake of clarity only selected curves are shown. In many cases results were nearly the same, as shown by two or more labels for one curve, or quite similar, as shown by a label in brackets. It should also be remembered that the predictions are the result of extending a crust and lithosphere of uniform initial thickness to give a final crustal thickness that, within the seismic constraints, is virtually indistinguishable among models. That there are any subsidence differences is due to additional processes that occur during rifting and cooling of the margin.

The models fail to predict sufficient subsidence of the Wyandot well by amounts ranging from 0.7 to 1.7 km. The necessary increase can most easily be achieved by increasing β from 1.10 to 1.15 ± 0.02 for the location of this well in the DD250 model, for example. Seismic constraints could not prohibit this change. Alternatively, if t_c had been ~38 km sufficient subsidence would be predicted without changing β. Equivalent increases could not be achieved solely by choosing a larger value of T_R, thereby increasing flexural downwarp, without affecting other shelf wells. A fourth possibility is that there was some erosion of the uplifted region created during rifting in the depth-dependent (DD) extension models. Were this the case, these models would have basement replaced by sediments, but the sedimentation could not occur until thermal subsidence and erosion levelled the topographic highs to sea-level. A model in which there was instantaneous erosion of basement uplifts above sea-level maximizes this effect and indicates that a segment ~0.7 km long, like that shown as a bold line, could be added to any of the DD models; DD250 was chosen, however, because it gave the best agreement with observed gravity anomalies. The age of the oldest sediment under these circumstances is difficult to model because the form that erosion may have taken is unknown, but it is unlikely that the onset of deposition could be delayed until ~16-Ma age as observed. A combination of small changes in β with erosion in the depth-dependent models, therefore, seems the most promising way to increase subsidence at the Wyandot well. In any case, the UE and UM models can be rejected because sediments had to be artifically withheld until ~160 Ma ago to prevent the basal sediments from being too old.

The DD250 model gave reasonably good results for the Fox well, but a slightly higher value of T_R would also be acceptable. The results suggest that the entire subsidence of this well is the result of flexure and that no thermal anomaly is predicted. The UE and UM models can again be rejected for the same reason as that for the Wyandot well. Furthermore, no significant erosion, leading to sedimentation of the form shown by the bold line, is required.

The results for the MicMac well suggest errors in the timing of early subsidence, otherwise agreement with the DD250 model is excellent. The total depth of sediments is unknown, the well having bottomed in the shallow water marine Mohawk Formation of Callovian age (Barss *et al.* 1979) which may be underlain by the Iroquois and Argo formations (Jansa & Wade 1975). The differences in observed and theoretical sediment age could be attributed to slow rates of early sedimentation or to a rifting process that was not complete until ~160 Ma ago, thereby lengthening the interval of initial subsidence and deposition of the syn-rift sediments from 185–175 Ma to 185–160 Ma. Clearly, the DD models cannot prevent early sedimentation for the MicMac well location because no uplift is predicted (Fig. 13) and the initial subsidence is the minimum possible for the value of β chosen. The advantage of slowing the initial subsidence and blending it with the thermal contraction subsidence (Jarvis & McKenzie 1980) is also suggested by the results from the Wyandot and Mississauga wells.

Apart from the hint of too rapid early subsidence, the age–depth relations predicted by the DD250 or UM250 models are in excellent agreement with the observations from the Mississauga well.

The Bluenose well results also indicate good agreement between observations and the DD250 model. This model has an early history similar to that of the UM250 and DD2-4R models but predicts deeper sediments for ages of $\gtrsim$100 Ma.

Observations from the Triumph well plot between the predictions of the DD250 (UM250, DD2–4R) group and DD0 suggesting that T_R may be a little less than 250°C. However, subtleties of sea-level and palaeobathymetry must be accounted for before this can be substantiated.

The results are generally in sufficiently good agreement with observations that it can be concluded that: (1) the choice of $\beta(x)$ is appropriate (with the possible exception of the Wyandot well); (2) flexural effects dominate thermal subsidence landward of the Wyandot well; and (3) no significant variations in the thickness of the crust or thermal lithosphere prior to rifting are necessary in order to explain the present age–depth relations along this profile. This point is important because the subsidence rate is sensitive to the lithospheric thermal time constant, $\tau = a^2/\pi^2\kappa$. Assuming κ to be constant, variations in 'a' of only ±20 per cent from the nominal value of 125 km would significantly perturb τ to 90 or 40 Ma from the 62.8 Ma value used, and these are values that would fail to give acceptable theoretical age–depth curves.

Having shown that the models predict reasonable present age–depth relationships, the model histories can be used to trace sediment burial, subsidence below sea-level, and temperature change. An example (Fig. 22) illustrates these theoretical results for a vertical section through the Triumph well (Figs 6 and 7) for depth-dependent extension models, T_R = 250°C, with and without radiogenic heat production. The vertical column at the right represents the model configuration at 185 Ma after rifting. Successive columns to the left illustrate progressively earlier configurations back to the time of rifting, 0 Ma. The long and short dashed lines show the development of the isotherm distribution for the models with and without radioactivity respectively. The 0°C isotherm is always the sediment–water interface, and therefore also illustrates the palaeobathymetry, which shows a steady shallowing for this particular well. The subsidence histories of sediments, solid lines labelled by their time of deposition since rifting, were similar for the two models and are therefore not differentiated in this example.

A comparison of the temperatures in this diagram with those of Fig. 19 shows that these are higher. Previous results somewhat underestimated sediment temperatures because sediment at 0°C is added at the end of each model timestep, not continuously throughout the

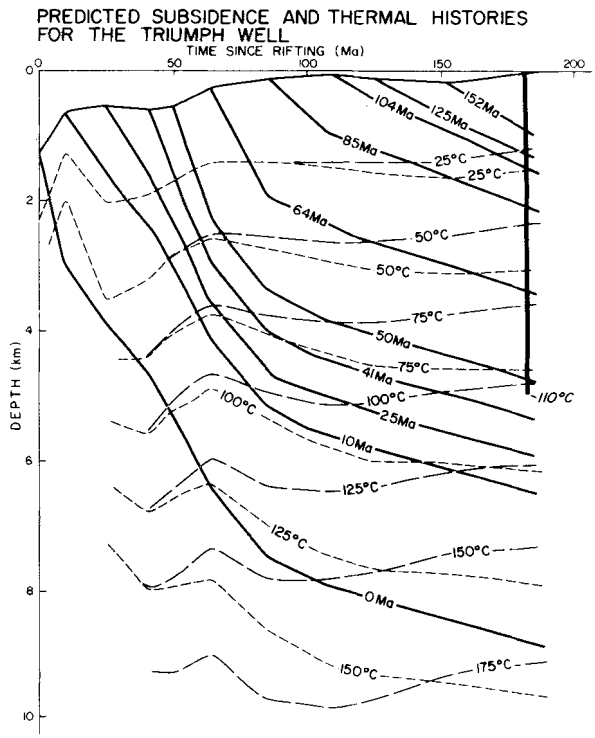

Figure 22. Predicted subsidence and thermal histories for a section through the Triumph P-50 deep exploratory well. The models are the depth-dependent extension models, T_R = 250°C, with and without radioactive heat generation (Fig. 19). The column furthest to the right represents the predicted present configuration with the bold solid lines indicating the age of the sediment and short and long dashed lines indicating predicted temperatures without and with radioactivity, respectively. The bold vertical line represents the Triumph well which had an observed bottom hole temperature of 110°C. Successive columns to the left represent the equivalent situation for progressively earlier times. Therefore, the bold solid lines trace the predicted subsidence histories of each of the stratigraphic horizons and are marked by their time of deposition measured from the time of rifting. Similarly, the dashed lines trace the temperature changes at depth with time. The 0°C isotherm, shown as a solid line, is also the water–sediment interface and its depth illustrates the changes in model palaeobathymetry for this location. The relationship between the subsidence curves and the isotherms describes the temperature histories of the sediments.

timestep. This has an effect that is approximately equal to the product of the thickness of the sediment for that timestep and the average sedimentary thermal gradient at that time and position. It could be correctly calculated by employing a predictor–corrector scheme in the thermal model integration in which the model thermal timestep is repeated and the sediments, as estimated by the present method, added continuously throughout the timestep. This was judged to be unnecessary because the amount of sediment added at each timestep is ~1 km giving rise to a correspondingly small bias in lithospheric temperatures. In the sediment region this bias is significant, therefore, it is assumed for the purpose of Fig. 22 that the thermal evolution kept pace with sedimentation and that sedimentation was continuous. This is clearly justified because the thermal time constant for the whole sediment column is < 1 Ma which is an order of magnitude less than the length of any of the model timesteps. The same argument cannot, however, be made for the whole lithosphere which has a thermal time constant of 62.8 Ma.

The most important property of Fig. 22 is that the temperature history of the sediments is given by the relationship of the subsidence to temperature curves. Such histories are directly related to the degree of thermal metamorphism of organic material within the sediments. The model predicts that all sediments are presently at their highest temperatures but that the temperature paths are not necessarily simple. There are differences between the predictions of the two models which become significant when it is recalled that metamorphism is a thermally activated process that proceeds as an exponential function of temperature.

The temperature measured at the base of the Triumph well was, as shown, 110°C (Royden & Keen 1980) in good agreement with the model with radioactivity. However, bottom hole temperatures from individual exploratory wells are notoriously inaccurate (Oxburgh 1980, private communication) and a better measure of accuracy may be a comparison of observed and predicted degree of thermal metamorphism of organic particles (Bostick 1973, Keen 1979 and Beaumont 1981). The present results are included merely to illustrate the potential of the calculations. They are not pursued further because the models were not designed for a detailed investigation of the sediments. A study of equivalent diagrams for other sections through the basin would, however, allow a crude prediction of the distribution of the oil and gas window for source beds which have retained their organic material.

10 Discussion and conclusions

10.1 MODEL RESULTS

An assessment of the results for the ~185 Ma old Nova Scotian margin indicates that a combination of the depth-dependent and uniform extension melt segregation rifting models would give the best agreement with observations. Landward of the hinge line depth-dependent extension provides the uplift necessary to delay early sedimentation, whereas lateral conduction of heat (Appendix A) probably gives insufficient uplift and with incorrect timing. The melt segregation model is the only one of the proposed rifting models that creates oceanic crust in a realistic manner. It is important, however, to note that the models exhibit a decaying sensitivity to the rifting processes as they evolve.

Gravity anomalies best constrain estimates of the thickness of the rheological lithosphere. If radiogenic heat and the possible existence of a brittle fracture near surface layer of the crust are ignored, the results indicate that 250°C should be chosen as the value of the relaxation isotherm. Under any circumstances a local model of isostatic equilibrium is inappropriate for this section of the Nova Scotian margin. If a fractured surface layer exists, and its depth is comparable to that created elsewhere during extension, the best choice for the relaxation isotherm is 450°C. The net thickness of the elastic core of the rheological lithosphere remains approximately the same as that for the earlier 250°C models. Beyond ~60 Ma after rifting the gravity anomalies are insensitive to the rifting process.

Depth-dependent extension models, with $T_R = 250°C$, and with or without radioactivity, give the overall best results for the stratigraphy of the model basin. This result does not place very strong constraints on the model parameters, however, because the true stratigraphy is not known in detail seaward of the shelf edge and it may be possible to bring some other models into agreement with observations by changing parameter values that were held constant during modelling. Consideration of radioactive heat generation within the crust and sediments does not substantially change the evolution of the basin or its associated gravity anomaly. The geothermal gradient is, however, increased leading to more realistic lower bound estimates of maximum temperatures within the basin of ~160°C as opposed to ~130°C without radioactivity.

It should be noted that for the choice of t_c, and other parameters (Table 1), the values of ρ_c and ρ_0 maximize the basin depth. This depth is relatively insensitive to other parameters such as a, α, T_m, K and A. That the basin may still be ~1 km too shallow is somewhat disconcerting under these circumstances. It must, however, be remembered that a uniform crustal thickness of 35 km was chosen based on estimates of the present crustal thickness at the landward end of the profile. Elsewhere in the Appalachian orogen crustal thicknesses of 40 km are common (Dainty *et al.* 1966; James, Smith & Steinhart 1968). Had $t_c = 38$ km been used, the basin would have been totally in accord with the estimates that exist. However, even these may be uncertain by ~ ±1 km (Fig. 7). Within this indeterminacy, observation and theory agree sufficiently well that the need for additional processes, such as phase changes, which may contribute to the tectonic subsidence cannot be demonstrated.

The model sedimentary basins differ appreciably from those predicted by more simple models in which the effects of sediment blanketing and a regional isostatic balance are ignored. The sediments cause two effects. They raise the average temperature of the whole model by thermal blanketing, thereby reducing the thermal contraction subsidence. Sediment loading also advects hot material ($T \simeq T_m$) through the base of the model. Its heat is then lost and is no longer available to contribute to the thermal contraction subsidence. The two effects taken together typically reduce the maximum basin depth by ~1.5 km with respect to the predicted depth were an old sediment-starved basin instantaneously filled. Lithospheric flexure reduces the maximum depth by a similar amount in comparison with $T_R = 0°C$ models. Consequently, the basin evolves to a maximum depth that is some 2.5–3.0 km less than would otherwise be predicted. This reduction in depth and the effect of changing geothermal gradients with radiogenic heat production may have important implications for sedimentary thermal metamorphism, as discussed in Section 9.

A sensitivity analysis demonstrates that subsidence of the basin and the final basin configuration are primarily determined by the parameters t_c, ρ_c, ρ_0, ρ_{sav}, β, and δ, where ρ_{sav} is the density of the compacted sediments averaged within the sediment column. Similarly, the rate of subsidence depends on the lithospheric thermal time constant, τ, and the loading history. Of these parameters β and δ were considered variables and the models were optimized with respect to them, subject to the constraints of present crustal thickness and the assumption of a uniformly thick crust before extension. Of the remaining parameters, the densities remain the most poorly determined and, as noted in the section on the rifting models, substantial changes in basin depth can be achieved by selecting other combinations of densities. The isostatic subsidence, is approximately proportional to $\phi_s = \rho_0'/(\rho_0' - \rho_{sav})$, the isostatic amplification factor, and initial subsidence is given by the analytical expressions in the section of rifting models. Therefore, the effect of choosing other densities can be approximately predicted without complete recalculation of the models. Values for the remaining parameters were taken from McKenzie (1978) in order to retain a consistent set with those already used extensively in the literature.

10.2 FUTURE WORK

A number of improvements to the models discussed in this paper are possible. These include the development of dynamical models of rifting in which rheological zonation of the lithosphere would be based on observations of micro-rheology (see, for example, Ashby & Verall 1977). Such models may demonstrate how pre-rift lithospheric structure and temperature distribution, and imposed strain rates influence the extension process (Vierbuchen, George & Vail 1981). An important question is whether the process can even be modelled by continuum mechanics or whether localized pre-existing inhomogeneities act as strain nucleation

sites, thereby distorting the otherwise predictable extension. The improved rheologies can also be introduced to the thermo-mechanical models. That the simple concepts already used provide fairly accurate results suggest that the improved rheology may only change the results in subtle ways. This is, however, a necessary step if realistic estimates of the stress distribution, caused by thermal evolution and isostatic adjustment at rifted margins, are to be made.

The thermal model can be made more rigorous by the inclusion of a predictor–corrector term, lateral heat transport, and a more detailed representation of the temperature distribution and thermal properties within the sediments. However, this may not improve the results significantly, or give the models greater predictive capabilities, because the question of the importance of convective as opposed to conductive heat transport within the sediments has not been addressed. It is already known that fluid circulation in the North Sea basin (Oxburgh 1980, private communication) and the Alberta basin (Majorowicz & Jessop 1981) among others is important and significantly modifies present geothermal gradients on both local and regional scales. Exactly how such circulation could be included in evolutionary models without an *a priori* knowledge of the basin structure is not clear. An improvement in our fundamental understanding of, and ability to model, thermal metamorphism of organic sediments is also necessary.

The universality of the model must also be tested by comparison with other rifted margins of differing ages and sediment regimes. It is unlikely, however, that the modelling will be as rewarding as that for the Nova Scotian margin because few, if any, rifted margins are as well studied. Variations in crustal thickness, for example, are presently known for very few transects. Young margins probably offer the best prospect because they should be the most sensitive to rifting history.

10.3 CONCLUSIONS

In summary, our conclusions are that:

(1) Extension models are successful in explaining the first-order processes that occurred during rifting of a section through the Nova Scotian continental margin.

(2) The thermo-mechanical model correctly predicts the large-scale development of this continental margin from rifting to the present.

(3) The development of the margin exhibits a fading memory of the details of the rifting process. However, a mechanism, like that provided by the depth-dependent extension model, is necessary in order to delay sedimentation on middle and inner shelf regions. Of the proposed rifting models, the uniform extension and melt segregation model provides the best explanation of the processes by which the transition from continental to oceanic crust at continental margins is created.

(4) The concept of a rheological lithosphere, bounded by isotherms and which responds elastically to loading, is useful in explaining departures from local isostatic equilibrium and the form of the free air gravity anomalies across the margin.

(5) The thermo-mechanical model predicts that thermal blanketing by sediments and departures from local isostatic equilibrium significantly reduce the maximum potential depth of rifted margin basins with respect to that predicted by more simple theory.

(6) The models predict reasonably accurate present age–depth relationships for deep exploratory wells adjacent to the section across the Nova Scotian margin. It is also believed that with additional small adjustments of model parameters the agreement could be made complete.

(7) Landward of the basin hinge line, subsidence is dominated by flexural downwarping, whereas seaward of the hinge line thermal effects predominate.

(8) The models are potentially capable of accurately tracing the subsidence history of sediments within the basin, and, in so far as conductive models of heat transport within the basin are correct, the models can also hindcast thermal histories for the sediments.

(9) Crustal and sedimentary radioactive heat production almost certainly plays a significant role in determining the temperature distribution within the sedimentary basin and, therefore by implication, the degree of thermal metamorphism of organic material within the sediments.

(10) The existence of a brittle crustal region which fails through listric normal faulting during extension cannot be proven from the model results. However, the results are certainly compatible with such an interpretation of the rheological lithosphere. Furthermore, the results (Fig. 20) provide an attractive starting point for a study of the behaviour of mature continental margins during subsequent ocean closure and continental collision.

Acknowledgments

We would like to thank Donna Nelson for her help in compiling much of the data for the cross-section of the Nova Scotian margin, John Wade for his advice on data interpretation, and Seiscan-Delta for permission to use previously unpublished seismic reflection data. Comments by Michael Keen, Garry Quinlan, Richard Haworth, and Jack Sweeney greatly helped improve the manuscript, for which we are grateful. Mary Wyman's patience in typing successive premature versions of the manuscript is also appreciated. Financial assistance for this study was provided by the Natural Sciences and Engineering Research Council, Canada through operating and strategic research grants to C. Beaumont.

References

Ashby, M. F. & Verall, R. A., 1977. Micromechanisms of flow and fracture and their relevance to the rheology of the upper mantle, *Phil. Trans. R. Soc. A*, **288**, 59–95.

Barrett, D. L. & Keen, C. E., 1976. Mesozoic magnetic lineations, the magnetic quiet zone, and seafloor spreading in the northwest Atlantic, *J. geophys. Res.*, **81**, 4875–4884.

Barss, M. S., Bujak, J. P. & Williams, G. L., 1979. Palynological zonation and correlation of sixty-seven wells, eastern Canada, *Pap. geol. Surv. Can. 78–24.*

Bathe, K. J., Wilson, E. L. & Iding, R. I., 1974. NONSAP a structural analysis program for static and dynamic response of nonlinear systems, Structural Engineering Laboratory, University of California, Berkeley, *report UC SESM 74–3.*

Beaumont, C., 1978. The evolution of sedimentary basins on a viscoelastic lithosphere: theory and examples, *Geophys. J. R. astr. Soc.*, **55**, 471–497.

Beaumont, C., 1979. On the rheological zonation of the lithosphere during flexure, *Tectonophys.*, **59**, 347–366.

Beaumont, C., 1981. Foreland basins, *Geophys. J. R. astr. Soc.*, **65**, 291–329.

Beck, A. E., 1976. An improved method of computing the thermal conductivity of fluid-filled sedimentary rocks, *Geophysics*, **41**, 133–144.

Berggren, W. A., 1972. A Cenozoic time scale – some implications for regional geology and paleobiogeography, *Lethaia*, **5**, 195–215.

Bostick, N. H., 1973. Time as a factor in thermal metamorphism of phytoclasts (coaly particles), *7th Cong. int. Stratigraphie et Geologie Carbonifere*, Krefeld, 1971, *C. r.*, **2**, 183–193.

Brown, C. & Girdler, R. W., 1980. Interpretation of African gravity and its implication for the break-up of continents, *J. geophys. Res.*, **85**, 6443–6455.

Bujak, J. P., Barss, M. S. & Williams, G. L., 1977a. Offshore eastern Canada – part 1. Offshore eastern Canada's organic type and colour and hydrocarbon potential, *Oil Gas J.*, **75**, 14, 198–202.

Bujak, J. P., Barss, M. S. & Williams, G. L., 1977b. Offshore eastern Canada – part 2. Organic type and colours and hydrocarbon potential, *Oil Gas J.*, **75**, 15, 96–100.

Dainty, A. M., Keen, C. E., Keen, M. J. & Blanchard, J. E., 1966. Review of geophysical evidence on crust and upper-mantle structure on the eastern seaboard of Canada, in *The Earth Beneath the Continents, Monogr. Am. geophys. Un.*, **10**, 349–369.

Eaton, G. P., 1979. Regional geophysics, Cenozoic tectonics, and geological resources of the Basin and Range Province and adjoining regions, Rocky Mountain Association of Geology, Utah Geological Association, *1979 Basin and Range Symp.*, pp. 11–39, eds Newman, G. W. & Goode, H. D.

Fairhead, J. D. & Reeves, C. V., 1977. Teleseismic delay times, Bouguer anomalies and inferred thickness of the African lithosphere, *Earth planet Sci. Lett.*, **36**, 63–76.

Given, M. M., 1977. Mesozoic and early Cenozoic geology of offshore Nova Scotia, *Bull. Can. Petrol. Geol.*, **25**, 63–91.

Hamilton, W. & Myers, W. B., 1966. Cenozoic tectonics of the western United States, *Rev. Geophys. Space Phys.*, **4**, 509–549.

Hamza, V. M. & Beck, A. E., 1975. Variations of heat flow and heat producing elements in sediments, *Can. J. Earth Sci.*, **12**, 996–1005.

Hyndman, R. D., Jessop, A. M., Judge, A. S. & Rankin, D. S., 1979. Heat flow in the Maritime provinces of Canada, *Can. J. Earth Sci.*, **16**, 1154–1165.

James, D. E., Smith, T. J. & Steinhart, J. S., 1968. Crustal structure of the Middle Atlantic States, *J. geophys. Res.*, **73**, 1983–2007.

Jansa, L. F., Bujak, J. P. & Williams, G. L., 1980. Upper Triassic salt deposits of the western North Atlantic, *Can. J. Earth Sci.*, **17**, 547–559.

Jansa, L. F. & Wade, J. A., 1975. Geology of the continental margin off Nova Scotia and Newfoundland, in *Offshore Geology of Eastern Canada, 2, Regional Geology, Pap. geol. Surv. Can. 74–30*, 51–105.

Jarvis, G. T. & McKenzie, D. P., 1980. Sedimentary basin formation with finite extension rates, *Earth planet. Sci. Lett.*, **48**, 42–52.

Keen, C. E., 1979. Thermal history and subsidence of rifted continental margins – evidence from wells on the Nova Scotian and Labrador shelves, *Can. J. Earth Sci.*, **16**, 505–522.

Keen, C. E., Beaumont, C. & Boutilier, R., 1982. A summary of thermo-mechanical model results for the evolution of continental margins based on three rifting processes, *Hedberg Research Conf.* of the American Association of Petroleum Geology, Galveston, in press.

Keen, C. E., Beaumont, C. & Boutilier, R., 1981. Preliminary results from a thermo-mechanical model for the evolution of Atlantic-type continental margins, in *Proc. 26th int. Geol. Congr., Geology of Continental Margins Symp.*, Paris 1980, *Oceanologica acta*, pp. 123–128.

Keen, C. E. & Cordsen, A., 1981. Crustal structure and seismic stratigraphy of the rifted continental margin off eastern Canada: Ocean bottom seismic refraction results off Nova Scotia, *Can. J. Earth Sci.*, **18**, 1523–1538.

Keen, C. E. & Hyndman, R. D., 1979. Geophysical review of the continental margins of eastern and western Canada, *Can. J. Earth Sci.*, **16**, 712–747.

Keen, C. E., Keen, M. J., Barrett, D. L. & Heffler, D. E., 1975. Some aspects of the ocean–continent transition at the continental margin of eastern North America, in *Offshore Geology of Eastern Canada*, eds Van der Linden, W. J. M. & Wade, J. A., *Pap. geol. Surv. Can. 74–30*, 189–197.

King, B. C. & Williams, L. A. J., 1976. The East African Rift System, in *Geodynamics: Progress and Prospects*, pp. 63–74, ed. Drake, C. L., American Geophysical Union.

Le Pichon, X. & Sibuet, J.-C., 1981. Passive margins: a model of formation, *J. geophys. Res.*, **86**, 3708–3720.

Lewis, J. F. & Hyndman, R. D., 1976. Ocean heat-flow measurements over the continental margins of eastern Canada, *Can. J. Earth Sci.*, **13**, 1031–1038.

Majorowicz, J. A. & Jessop, A. M., 1981. Regional heat flow patterns in the Western Canadian Basin, *Tectonophys.*, **74**, 209–238.

McIver, N. L., 1972. Cenozoic and Mesozoic stratigraphy of the Nova Scotian shelf, *Can. J. Earth Sci.*, **9**, 54–70.

McKenzie, D. P., 1978. Some remarks on the development of sedimentary basins, *Earth planet. Sci. Lett.*, **40**, 25–32.

Montadert, L., de Charpal, O., Roberts, D., Guennoc, P. & Sibuet, J.-C., 1979. Northeast Atlantic passive continental margins: rifting and subsidence processes, in *Am. geophys. Un., M. Ewing Symp.*, Series 3, 154–186.

Okabe, M., 1979. Analytical expressions for gravity anomalies due to homogeneous polyhedral bodies and translations into magnetic anomalies, *Geophysics*, **44**, 730–741.

Panza, G. F., Mueller, St & Calcagnile, G., 1982. The gross features of the lithosphere–asthenosphere system in the European Mediterranean area, *Phys. Earth planet. Int.*, in press.

Parker, R. L. & Oldenburg, D. W., 1973. Thermal model of ocean ridges, *Nature Phys. Sci.*, **242**, 137–139.

Parsons, B. & Sclater, J. G., 1977. An analysis of the variation of ocean floor bathymetry and heat flow with age, *J. geophys. Res.*, **82**, 803–827.

Peltier, W. R., 1974. The impulse response of a Maxwell earth, *Rev. Geophys. Space Phys.*, **12**, 649–669.
Proffett, J. M., Jr, 1977. Cenozoic geology of the Yerington district, Nevada, and implications for the nature and origin of Basin and Range faulting, *Bull. geol. Soc. Am.*, **88**, 247–266.
Purcell, L. P., Rashid, M. A. & Hardy, I. A., 1979. Geochemical characteristics of sedimentary rocks in Scotian Basin, *Bull. Am. Ass. Petrol. Geol.*, **63**, 87–105.
Robbins, E. I. & Rhodehamel, E. C., 1976. Geothermal gradients help predict petroleum potential of Scotian Shelf, *Oil Gas J.*, **74**, 9, 143–145.
Royden, L. & Keen, C. E., 1980. Rifting process and thermal evolution of the continental margin of eastern Canada determined from subsidence curves, *Earth planet. Sci. Lett.*, **51**, 343–361.
Royden, L., Sclater, J. G. & Von Herzen, R. P., 1980. Continental margin subsidence and heat flow, important parameters in formations of petroleum hydrocarbons, *Bull. Am. Ass. Petrol. Geol.*, **64**, 173–187.
Rubey, W. W. & Hubbert, M. K., 1960. Role of fluid pressure in mechanics of overthrust faulting, II overthrust belt in geosynclinal area of western Wyoming in light of fluid pressure hypothesis, *Bull. geol. Soc. Am.*, **60**, 167–205.
Sclater, J. G. & Christie, P. A. F., 1980. Continental stretching: an explanation of the post Mid-Cretaceous subsidence of the Central North Sea Basin, *J. geophys. Res.*, **85**, 3711–3739.
Sclater, J. G., Royden, L., Horvath, F., Burchfiel, B. C., Semkin, S. & Stegena, L., 1980. Subsidence and thermal evolution of the intra-Carpathian basins, *Earth planet. Sci. Lett.*, **51**, 139–162.
Sheridan, R. E., Grow, J. A., Berhendt, J. C. & Bayer, K. C., 1979. Seismic refraction study of the continental edge of the Eastern United States, *Tectonophys.*, **59**, 1–26.
Shih, K. G., MacNab, R. & Halliday, D., 1981. Multiparameter survey data from the Scotian Margin, *Geol. Surv. Can., Open File 750.*
Sleep, N. H., 1971. Thermal effects of the formation of Atlantic continental margins by continental break-up, *Geophys. J. R. astr. Soc.*, **24**, 325–350.
Van Hinte, J. E., 1976a. A Jurassic time scale, *Bull. Am. Ass. Petrol. Geol.*, **60**, 489–497.
Van Hinte, J. E., 1976b. A Cretaceous time scale, *Bull. Am. Ass. Petrol. Geol.*, **60**, 498–516.
Vierbuchen, R. C., George, R. P. & Vail, P. R., 1981. A thermal-mechanical model of rifting with implications for outer highs on passive continental margins, *Prog. Abstr., Hedberg Research Conf.*, p. 63, American Association of Petroleum Geology, Galveston.
Watts, A. B., 1978. An analysis of isostasy in the world's oceans: Part 1 – Hawaiian–Emperor seamount chain, *J. geophys. Res.*, **83**, 5989–6004.
Watts, A. B. & Ryan, W. B. F., 1976. Flexure of the lithosphere and continental margin basins, *Tectonophys.*, **36**, 25–44.
Watts, A. B. & Steckler, M. S., 1979. Subsidence and eustasy at the continental margin of eastern North America, in *Am. geophys. Un., M. Ewing Symp.*, Series 3, 218–234.
Weertman, J., 1970. The creep strength of the Earth's mantle, *Rev. Geophys. Space Phys.*, **8**, 145–168.

Appendix A

The effects of perturbations from lateral heat conduction on the models were computed by representing the thinned lithosphere as a two-dimensional parallelepiped of maximum thickness a and width b (Fig. A1). Analytical solutions to the equation of heat conduction in two dimensions,

$$\frac{\partial^2 T}{\partial x^2} + \frac{\partial^2 T}{\partial z^2} = \frac{1}{\kappa}\frac{\partial T}{\partial t}$$

were obtained, subject to the bottom boundary condition; $z = 0$, $T = T_m$; and upper boundary condition $z = a$, $T = 0$. The ends of the slab, $x_0 = 0$ and $x_K = b$ were assumed to be sufficiently far from any horizontal variations in the initial temperature distribution that $\partial T/\partial x = 0$ at those points.

The slab was divided into K regions (Fig. A1), each of which is characterized by an initial temperature distribution, $T_i(z, 0)$, $i = 1 \ldots K$. These initial conditions are determined by specifying the extension parameter β_i (and δ_i) in each region. In this manner the initial temperature distribution immediately after rifting is approximated by isotherms which have a step-like appearance.

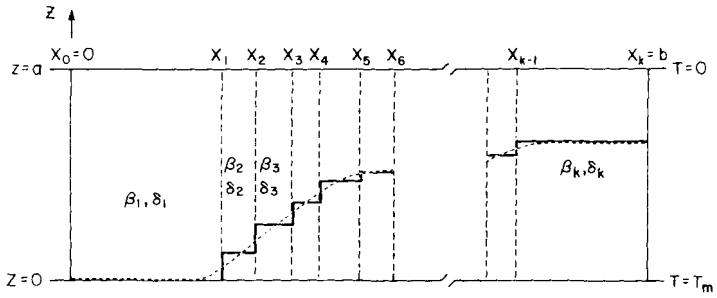

Figure A1. Model used for two-dimensional heat flux calculations (see text for further details).

The solution to the equations of heat conduction has the form

$$T^*(x, z, t) = \sum_{n=1}^{\infty} \sum_{m=0}^{\infty} A_{nm} \sin \frac{n\pi x}{a} \cos \frac{m\pi x}{b} \exp(-\kappa \alpha_{nm}^2 t)$$

where

$$A_{nm} = \frac{4}{ab} \int_0^b \int_0^a T^*(x, z, 0) \sin \frac{n\pi z}{a} \cos \frac{m\pi x}{b} \, dz \, dx,$$

$$\alpha_{nm}^2 = \pi^2 \left(\frac{n^2}{a^2} + \frac{m^2}{b^2} \right),$$

and $T^*(x, z, t)$ is the temperature excess over the equilibrium temperature.

The form of $T^*(x, z, 0)$, the initial temperature distribution, is known. It is a function of the extension parameters β(and δ) in each of the K intervals. Therefore, the Fourier coefficients, A_{nm}, can be evaluated,

$$A_{nm} = \frac{4}{ab} \sum_{i=1}^{K} \int_{x_{i-1}}^{x_i} \left[\int_0^a T_i^*(z, 0) \sin \frac{n\pi z}{a} \, dz \right] dx.$$

The inner integrals are directly related to the one-dimensional solutions for the Fourier coefficients for uniform and non-uniform extension (Royden & Keen 1980).

$$\int_0^a T_i^*(z, 0) \sin \frac{n\pi z}{a} \, dz \equiv \gamma_{in}(\delta_i, \beta_i)$$

$$= \frac{a}{n^2 \pi^2} T_m [(\beta_i - \delta_i) \sin(n\pi \{1 - d/a\beta_i\}) + \delta_i \sin(n\pi \{1 - d/a\beta_i - (1 - d/a)/\delta_i\})].$$

Evaluation of the integral over x gives,

$$A_{nm} = \frac{4}{m\pi a} \left[\sum_{i=1}^{K} \gamma_{in} \left(\sin \frac{m\pi x_i}{b} - \sin \frac{m\pi x_{i-1}}{b} \right) \right].$$

The elevation above the final equilibrium level at $t \to \infty$ due to initial heating is given by

$$U(x, t) = \alpha \int_0^a T^*(x, z, t) \, dz$$

where the relationship between U, and subsidence, S, is $S(x, t) = U(x, 0) - U(x, t)$. This gives

$$U(x, t) = \frac{2\alpha a}{\pi} \sum_{n=1}^{\infty} \sum_{m=0}^{\infty} \frac{A_{m,2n-1}}{2n-1} \cos\frac{m\pi x}{b} \exp(-\kappa \alpha_{m,2n-1}^2 t).$$

Numerical values for $U(x, t)$ can be compared to one-dimensional solutions, $U_1(t)$, using the same values of β (and δ). The difference between them, $\Delta U = u(x, t) - U_1(t)$, is a measure of the effects of lateral heat conduction on the subsidence history for a particular region of the model, characterized by $\beta_i(x)$ and $\delta_i(x)$.

Solutions were obtained for ΔU using the $\beta(x)$ and $\delta(x)$ distributions for the uniform and depth-dependent extension models across the Nova Scotian margin. A total width of b = 700 km was assumed in the calculations and other physical properties of the model were the same as those used elsewhere in this paper. The margin was divided into 16 regions, which allowed a good approximation to the initial temperature distribution. The regions varied in width from about 200 km at the extreme ends of the model of 12–30 km where significant lateral changes in initial temperature occur. Both models produced similar results and Fig. A2 shows the behaviour of ΔU for the depth-dependent extension model, for which the initial temperature distribution is shown in Fig. 13. About 120 m of uplift is produced in about 60 Ma by heating of the region landward of the hinge line, due to lateral heat transfer from regions of the model where β, δ and the temperatures are greater. This uplift was produced at the expense of the outer shelf and slope region, where additional tectonic subsidence of the same magnitude occurred. The effects of lateral heat conduction first increase, and then decrease with time as shown in Fig. A2.

Comparable results were obtained for a narrower margin, where only 66 km separates unmodified continental crust from oceanic crust. However, the magnitude of ΔU is greater; reaching a maximum uplift of about 350 m just landward of the hinge line and a minimum of 200 m beneath of outer shelf. The shape of the $\Delta U(x, t)$ curves similar to those shown in Fig. A2, except that the region over which ΔU is significantly different from zero is less.

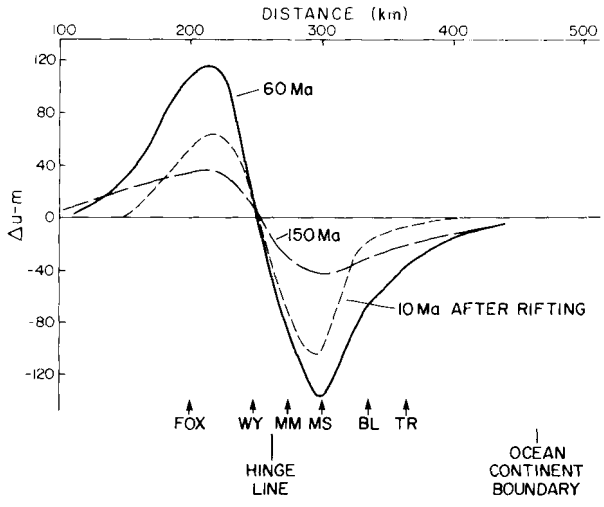

Figure A2. Plots of ΔU (m) showing the deviation in uplift from that predicted by the depth-dependent extension model, T_R = 250°C (Figs 13, 14 and 15), when lateral heat flux is included, as a function of position across the margin. This deviation is shown for three times after rifting. The positions of the deep exploratory wells are also shown.

It is unlikely that neglect of lateral heat conduction causes significant errors in the models. Lateral heat conduction will produce more subsidence (up to ~300 m with sediment) beneath the basin during its evolution, but this will be small after 185 Ma. It produces uplift landward of the hinge line, which increases in the first 60 Ma and would affect the stratigraphy in that region. In the early stages ($\lesssim 60$ Ma) of evolution, it could be a contributory mechanism for the apparent uplift of that region. It is unlikely to be the dominating factor, however. Wells such as Wyandot, situated near the hinge line, could not have experienced appreciable uplift due to lateral heat conduction; yet as discussed in the text that well was apparently above sea-level until about 25 Ma after rifting. Also, as shown in Fig. 21, the Wyandot well exhibits rapid subsidence as soon as it sinks below sea-level. If uplift were due to lateral heat conduction only, slow subsidence would be expected after submergence, as the seaward load of sediment produced sufficient flexure to overcome uplift. Finally, uplift due to lateral conduction of heat, cannot sufficiently inhibit early subsidence in the face of flexure in the region of Wyandot and Fox wells, suggesting a requirement for depth-dependent extension in that region of the model.

Appendix B

B.1 THE DEPTH-DEPENDENT EXTENSION MODEL WITH RADIOACTIVE HEAT GENERATION

The model parameters are the same as those described in Section 3 with the exception that a near surface crustal layer, thickness b km ($b \leqslant d \leqslant t_c$, z measured positive downward from the surface), with a uniform concentration of radiogenic heat, production rate A per unit volume, is assumed to exist prior to extension (Fig. B1). Since $b \leqslant d$ the radiogenic region is thinned by β during extension, whereas $z > d$ is thinned by δ as before. Other thermal properties are assumed to be uniform throughout the model.

The equilibrium temperature distribution with depth is given by the solution of

$$\frac{d^2T}{dz^2} = -\frac{A}{K}$$

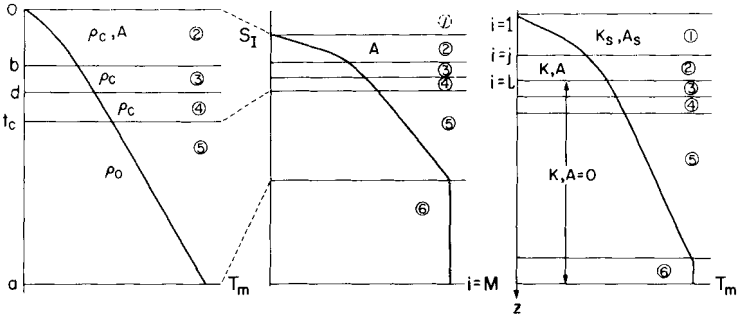

Figure B1. One-dimensional diagrams of initial and thermal subsidence of the depth-dependent rifting model that includes crustal and sedimentary radioactive heat production. The column to the left shows the pre-rift configuration which has a layer of depth b in which there is uniform heat production, A. Other symbols are as previously defined. b is less than d, therefore, the radioactive region is thinned by β during rifting (central column). Sedimentation and thermal subsidence depress this layer with time and radioactive sediments of mean thermal conductivity, K_s, and radiogenic heat production, A_s, are added (right-hand column). Both K_s and A_s in any sedimentary column are weighted means determined from the lithology and appropriate sediment properties (Table 1).

subject to the boundary conditions $T(z=0) = 0°C$ and $T(z=a) = T_m$. Temperature and its gradient are also continuous across the interface at $z = b$. The solution is

$$T(z) = -\frac{Az^2}{2K} + \left(\frac{T_m}{a} - \frac{Ab^2}{2Ka} + \frac{Ab}{K}\right) z \qquad 0 \leqslant z \leqslant b$$

$$= \left(\frac{T_m}{a} - \frac{Ab^2}{2Ka}\right) + \frac{Ab^2}{2K} \qquad b \leqslant z \leqslant a.$$

To determine the initial subsidence (S_I) through a calculation of the isostatic balance between extended and unextended regions, it is necessary to calculate the average densities (ρ_{av}) in each of the regions of Fig. B1. These are related to the average temperatures (T_{av}) of these regions by relationships of the type $\rho_{av} = \rho_{0av}(1 - \alpha T_{av})$, where ρ_{0av} is the average density at $T = 0°C$ and α is the volume coefficient of thermal expansion. The average temperature for the region $0 \leqslant z \leqslant d$ is

$$T_{23av} = \left(\int_0^d T(z)\, dz\right) \Big/ d,$$

which yields

$$T_{23av} = \left(\frac{T_m}{2a} - \frac{Ab^2}{4Ka}\right) d + \frac{Ab^2}{2K} - \frac{Ab^3}{6Kd}.$$

Similar relationships hold for regions 4 and 5,

$$T_{4av} = \left(\frac{T_m}{2a} - \frac{Ab^2}{4Ka}\right)(t_c + b) + \frac{Ab^2}{2K}$$

$$T_{5av} = \left(\frac{T_m}{2a} - \frac{Ab^2}{4Ka}\right)(t_c + a) + \frac{Ab^2}{2K}.$$

These average temperatures and corresponding average densities are preserved on extension so that the isostatic balance is given by

$$d\rho_{c23av} + (t_c - d)\,\rho_{c4av} + (a - t_c)\rho_{0av} = \frac{d}{\beta}\rho_{c23av} + \left(\frac{t_c - d}{\delta}\right)\rho_{c4av} + \left(\frac{a - t_c}{\delta}\right)\rho_{0av}$$

$$+ \left(a - \frac{d}{\beta} - \frac{a-d}{\delta} - S_I\right)\rho_0',$$

where the densities are the pre- and post-rift average densities of the regions 2–5 and $\rho_0' = \rho_0(1 - \alpha T_m)$. Rearrangement gives the initial subsidence,

$$S_I[\beta(x), \delta(x), t = 0^+] = a\left(1 - \frac{1}{\delta}\right) + d\left(\frac{1}{\delta} - \frac{1}{\beta}\right)$$

$$- \left[d\rho_{c23av}\left(1 - \frac{1}{\beta}\right) + [(t_c - d)\,\rho_{c4av} + (a - t_c)\,\rho_{0av}]\left(1 - \frac{1}{\delta}\right)\right] \Big/ \rho_0'.$$

The asymptotic thermal contraction subsidence $S_C[\beta(x), \delta(x), t \to \infty]$ is given by

$$(a - S_I)(1 - \alpha T_{iav}) = (a - S_I - S_C)(1 - \alpha T_{fav}), \qquad \text{(B1)}$$

where T_{iav} and T_{fav} are the initial ($t = 0^+$) and final ($t \to \infty$) average temperatures of the extended region and α is assumed uniform throughout the model. This relationship simply demonstrated that the initial post-rift and final states would have the same lithospheric thickness were they cooled to 0°C.

$$T_{iav} = \frac{1}{a - S_I} \int_0^{a - S_I} T(\delta, \beta, z, t = 0^+)\, dz$$

$$= T_m - \frac{1}{a - S_I} \left\{ \left(T_m - \frac{Ab^2}{2K} \right) \left[\frac{d}{\beta} \left(1 - \frac{d}{2a} \right) + \frac{a - d}{2\delta} \left(1 - \frac{d}{a} \right) \right] - \frac{Ab^3}{6K\beta} \right\}.$$

Calculation of T_{fav} is more complicated because the position of the base of the radiogenic region and, therefore, the modified radiogenic production rate per unit volume cannot be determined *a priori* because they are functions of the temperature distribution. An iterative solution initially assumes that there is no thermal contraction of the radiogenic region; that is, the interface remains at $z = b/\beta = b'$. The first estimate of the average temperature of each region is then determined in the same way as the pre-extension distribution. When integrated this gives

$$T_{fav}^{(1)} = \frac{T_m}{2} + \frac{Ab'^2}{4K} - \frac{Ab'^3}{6Ka'},$$

where

$$a' = (a - S_I - S_0) = (a - S_I)\,(1 - \alpha T_{iav})/(1 - \alpha T_{fav}) \tag{B2}$$

from (B1). Substituting for T_{iav}, T_{fav} and $S_C = a - S_I - a'$ in (B2) and rearranging gives

$$S_C[\beta(x), \delta(x), t \to \infty) = \frac{\alpha}{2 - \alpha(T_m + Ab^2/2K\beta^2)} \left\{ \left(T_m \frac{Ab^2}{2K\beta^2} \right)(a - S_I) + \frac{Ab^3}{3K\beta} \left(1 - \frac{1}{\beta^2} \right) \right.$$

$$\left. - 2 \left(T_m - \frac{Ab^2}{2K} \right) \left[\frac{d}{\beta} \left(1 - \frac{d}{2a} \right) - \left(\frac{a - d}{2\delta} \right) \left(1 - \frac{d}{a} \right) \right] \right\}.$$

An estimate of the error that results from ignoring thermal contraction of the radiogenic region is found from the thermal contraction using $T_f^{(1)}(z)$, the first estimate of the final temperature disttribution. For example, the decrease in the average temperature of the radiogenic region for $\beta = 5.4$ is ~ 35°C, changing b' by 2.0 m. If this improved estimate of b' were used, the new estimate of S_C would increase by 3.7 mm. It can be seen that the first approximation was justified and that (B2) is sufficiently accurate.